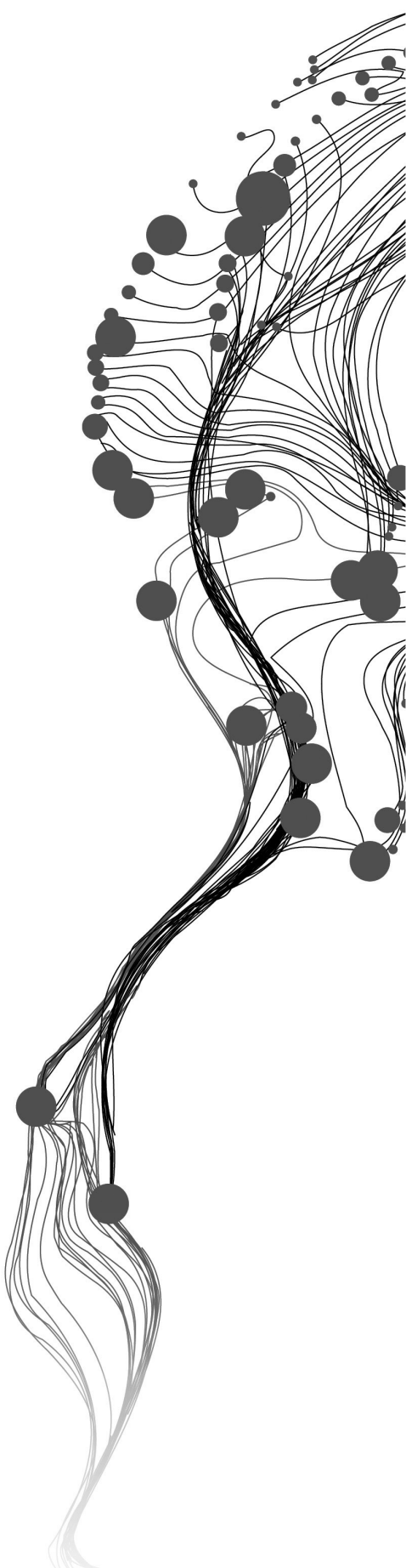


MAPPING RIFT TECTONICS USING GESTALT PSYCHOLOGY AND STATISTICS

DAFNI SIDIROPOULOU VELIDOU
March, 2014

SUPERVISORS:

Dr. T. Woldai
Dr. V.A. Tolpekin, Prof. Dr. Ir. A. Stein



MAPPING RIFT TECTONICS USING GESTALT PSYCHOLOGY AND STATISTICS

DAFNI SIDIROPOULOU VELIDOU
Enschede, The Netherlands, March, 2014

Thesis submitted to the Faculty of Geo-information Science and Earth
Observation of the University of Twente in partial fulfilment of the requirements
for the degree of Master of Science in Geo-information Science and Earth
Observation.
Specialization: Geoinformatics

SUPERVISORS:

Dr. T. Woldai
Dr. V.A. Tolpekin, Prof. Dr. Ir. A. Stein

THESIS ASSESSMENT BOARD:

Dr. Ir. M.G. Vosselman (chair)
Ir. G.N. Parodi

Disclaimer

This document describes work undertaken as part of a programme of study at the Faculty of Geo-information Science and Earth Observation of the University of Twente. All views and opinions expressed therein remain the sole responsibility of the author, and do not necessarily represent those of the Faculty.

ABSTRACT

Automatic geological lineament mapping is a task related to edge detection, since these structures are linear features that appear as such on satellite images. There have been many efforts to establish an automatic method, as field studies are time consuming and costly. All those efforts involve the use of a standard edge detection algorithm.

This study is a research on the application of a novel edge detection method for automatic geological lineament mapping from remotely sensed data. This method is based on models of human visual perception described by Gestalt theory and incorporates them in the line detection process. The Helmholtz principle is a new condition introduced in the method that distinguishes the detections into those that represent real object images and false ones. Segment detection algorithms based on these principles have been applied the last years in ordinary images. This research explores the use of such an algorithm in order to solve a Geo-information problem.

The applied method starts with a classic line segment detection based on the image gradient. In the next step, all the detected segments are evaluated on the basis of a probabilistic model of the Helmholtz principle and only those that prove to not be result of noise (artefacts) are accepted. This research explored the optimal values of the internal algorithm parameters that best suit the particular application. For this purpose, a novel validation method was developed. The method considers distance and local orientation measures for the comparison of the result with a reference dataset. The outcome of the validation method was a description of the error patterns, false and missing detections, for several parameter values. The optimal values were selected by combining the validation results with visual interpretation.

Some of the optimal parameter values proved to be different from the ones used in ordinary images. The reason is the nature of the geological edges and their appearance on Remotely Sensed data. Lineaments are fuzzy edges, whose gradient angle is more noisy than this of solid lines on close-range imagery. Another challenge of edge detection in this application is the distinction between the actual lineament and the opposite edge of the crusting, which along with the lineament define the fault scarp. The presence of the scarp on the images many times results in the detection of narrow polygon features which deviate from clear lines.

The relationship of the detected segments with the lines delineated in the reference dataset was explored on the basis of a detailed analysis. Anisotropy was observed in the distribution of detected segment's points along the two sides of the reference lineaments, which was explained by the appearance of the lineament and its associated slope on the image.

The geometrical characteristics of the current detection can be exploited towards the establishment of a relationship between the appearance of geological lineaments on satellite images and the product of visual interpretation and geological experience. Subjectivity in geological interpretation remains a challenge related to the certainty of automatic detection results.

The imagery used in this study was an ASTER scene of the Lake Magadi area in Kenya. The algorithm was developed in the open source platform R.

Keywords

Gestalt theory, Helmholtz principle, Automatic lineament mapping

ACKNOWLEDGEMENTS

After this one year and a half I would like to thank all the people from who I learned and worked with for the completion of this course and the thesis. First, I would like to thank my supervisors for their help and for turning these last six months of my studies into an interesting learning process and an enjoyable experience.

My family, for giving me the freedom of choice all the way and the chance to follow this course. My brother for being a source of inspiration.

I would also like to thank all my friends in Greece and all around Europe for sharing my good and hard times.

TABLE OF CONTENTS

Abstract	i
Acknowledgements	ii
1 Introduction	1
1.1 Background	1
1.2 Problem Statement and Motivation	2
1.3 Research identification	2
1.3.1 Research objectives	2
1.3.2 Research questions	2
1.4 Research Approach	3
1.5 Thesis structure	3
2 Literature review	5
2.1 Gestalt theory and the Helmholtz principle	5
2.2 Number of False Alarms and Meaningful Alignments	5
2.3 Related work	6
2.4 Automatic lineament mapping	6
2.5 Evaluation of automatically extracted features	7
3 Data	9
3.1 Study area	9
3.2 Images	10
3.3 Reference data	11
4 Method	13
4.1 Segment detection algorithm	13
4.1.1 Multispectral data	13
4.1.2 Image scaling	13
4.1.3 Gradient computation	14
4.1.4 Gradient ordering and threshold	15
4.1.5 Region growing	15
4.1.6 Rectangle approximation	16
4.1.7 Number of False Alarms (NFA) calculation	17
4.2 Parameter tuning and validation	18
4.2.1 Interval points on reference lines	19
4.2.2 Local orientation of detected points	20
4.2.3 Distance measures and accuracy assessment	21
4.2.4 Implementation	23
4.3 Assessment of the detected segments	24

5	Results	27
5.1	Introduction	27
5.2	Tuning of scale parameter	27
5.3	Tuning of angle tolerance	29
5.4	Scale factor revisited	32
5.5	Tuning of the NFA threshold parameter ε	32
5.6	Accuracy of the result	34
5.7	Error visualization	36
5.8	Detailed assessment of the detected segments	38
6	Discussion	47
6.1	Lineaments on remotely sensed images	47
6.2	Uncertainty in lineament interpretation and automatic detection	48
6.3	Validation method	49
6.4	Computational efficiency	51
7	Conclusions & Recommendations	53
7.1	Parameter tuning	53
7.2	Assessment of the detection results	53
7.3	Recommendations	54

LIST OF FIGURES

3.1	Location of the study area	9
3.2	ASTER Image	10
3.3	Reference lineament map	11
3.4	Rose diagram of the lineaments in the reference dataset	12
3.5	Graben and horst structures	12
4.1	Gradient calculation mask	14
4.2	Level-line angle	14
4.3	Gradient Images	15
4.4	Line-support region	16
4.5	Illustration of PCA transformation	17
4.6	Associated rectangles and NFA	18
4.7	Meaningful Segments	19
4.8	Interval points and local orientation	20
4.9	Reference lines and interval points	21
4.10	Local angle calculation of detected points	22
4.11	Detected segment and corresponding reference line	24
4.12	Intersection of lineament with detected segment	25
5.1	Algorithm parameters in 2D and 3D space	28
5.2	Ratio of missing and false detections for varying scale factor S	29
5.3	Scale factor tuning	30
5.4	Missing and false detections' ratio for varying angle tolerance (τ°)	32
5.5	Angle tolerance tuning	33
5.6	Illustration of the final angle tolerance value	34
5.7	Missing and false detections' ratio for varying scale factor S and $\tau = 25^\circ$	36
5.8	Scale factor tuning check	37
5.9	Missing and false detections' ratio for varying ε	38
5.10	NFA threshold tuning	39
5.11	Final detection result	40
5.12	Histogram of the distances	41
5.13	Successful and Missing detections	42
5.14	True and False detections	43
5.15	Regions of missing and false detections	44
5.16	Scale factor and point distribution	44
5.17	Angle tolerance and point distribution	45

LIST OF TABLES

3.1	Spectral range of ASTER VNIR bands	10
5.1	Scale factor variation	28
5.2	Angle tolerance (τ) variation	31
5.3	Scale factor variation for the fixed value $\tau = 25^\circ$	34
5.4	ε variation	35
5.5	ε and number of ε -meaningful segments	35
5.6	Mean and standard deviation of distances	36
5.7	Scale factor and distribution of extracted points	39
5.8	Angle tolerance and distribution of extracted points	41

Chapter 1

Introduction

1.1 BACKGROUND

In image processing and computer vision we refer to edges as discontinuities in the pixel intensities. Edge detection deals with the tracking and identification of abrupt changes in the grey values of the image (Ziou and Tabbone, 1998). The product is an edge map which usually constitutes an intermediate product for automatic object extraction.

Several edge detection algorithms have been developed and the majority of them uses linear models to identify those changes in the brightness values (Khomyakov, 2012). Two main categories of linear edge detection algorithms are gradient and second order derivative operators. Sobel, Prewitt, Roberts, Robinson, Kirsch and Laplacian or LOG (Laplacian on Gaussian) are examples of the first and the second category respectively. Furthermore, several methods that are based on the Hough transform, which is a feature extraction technique, have been proposed (Guru et al., 2004). Moreover, a widely used algorithm is the one presented originally by Burns et al. (1986) and explores the gradient magnitude and orientation of the pixels for edge detection.

Most edge detection algorithms encounter difficulties. The main issue is the effect of noise in the images, which obstructs the task of the operator. For this reason, several algorithms perform smoothing of the image for noise reduction before the actual edge detection. Such smoothing has a significant negative effect on the image, that of information loss (Ziou and Tabbone, 1998), since the discontinuity in magnitude is reduced. Inability to detect the edge direction, double edges, false and missing true detections often occur and restrict the performance of the algorithms.

Recent work (Desolneux et al., 2001; Grompone von Gioi et al., 2012) in edge detection for image processing is based on Gestalt theory and the Helmholtz principle. Gestalt theory is a scientific effort to describe the laws of human visual reconstruction. Similarly, the Helmholtz principle explains when individual geometrical structures form a single object, based on a single quality, e.g. color (Desolneux et al., 2000). Desolneux et al. (2008) described these laws in terms of a probabilistic model that could be used in computer vision and image analysis.

The advantage of using this theory for edge detection is that no *a priori* knowledge is needed and that a Number of False Alarms (NFA) can be computed. According to a basic principle of perception due to Helmholtz, a geometric element is defined as “meaningful” if it would hardly ever occur in a randomly created image (Desolneux et al., 2001). This brings us back to the main problem of edge detection algorithms, the noise. In practice, in a noisy image with no line segments present, a detection algorithm could return as a result a structure that is not really there. NFA is a variable that can be used to prevent this kind of errors, by considering the expectation of the number of occurrences of the detected event (Desolneux et al., 2008, chap.3)

1.2 PROBLEM STATEMENT AND MOTIVATION

Application of edge detection is relevant for geological interpretation and lineament extraction from remotely sensed data. The term geological lineament has been defined by several authors. Hobbs (1904) proposed the term lineament for linear forms of the landscape triggered by joints and faults, that reveal the architecture of the rock basement. O'Leary et al. (1976) defined the lineaments as "a mappable, simple or composite linear feature of a surface, whose parts are aligned in a rectilinear or slightly curvilinear relationship" which indicates a phenomenon below the surface. This definition has been widely used in the coming years (Hung et al., 2005; Thannoun, 2013). In the same lines, Clark and Wilson (1994) described lineaments as linear features on the surface, that depict a geological or geomorphological phenomena. More recently, Vassilas et al. (2002) expressed lineaments in terms of an image, as lines or linear formations with pixels that have prevailing intensities as compared to the background.

In situ geological surveys for lineament mapping involve drilling and the use of geophysical data. There the cost is high and the full extraction of geological structures is not guaranteed, unless high resolution data is available. Therefore, the use of remote sensing for automatic lineament extraction is preferred (Hung et al., 2005). Several algorithms have been used and tested in satellite images for automatic lineament extraction (Karnieli et al., 1993; Lee and Moon, 2002). Examples are the Canny algorithm, Laplacian, Ford, directional filters, Sobel and Kirsch operators and Rothwell edge detector (Mavrantza and Argialas, 2002).

The aim of the present research is to apply an edge detection algorithm based on Gestalt theory and the Helmholtz principle for the task of automatic geological lineament extraction, from remotely sensed data. It is intended to introduce this method for Remote Sensing problems and particularly automatic geological lineament mapping. Several parameters and functions of the algorithm are tuned and adjusted in order to comply with the the properties of the phenomenon to be mapped and the characteristics of the image. Finally, a method to assess the quality of the extraction results is developed and it is examined whether this method is suitable for this application.

1.3 RESEARCH IDENTIFICATION

The present study aims at implementing and testing the potential of a line segment detection algorithm based on Gestalt theory and the Helmholtz principle for a problem of Remote Sensing, that of automatic geological lineament mapping. The main objective is to examine the performance of such an algorithm for the detection of geological structures on a satellite image and improve the method accordingly to better serve the data and the purpose. The research objectives and questions are listed below.

1.3.1 Research objectives

- Adjust and extend a line segment detection algorithm, based on Gestalt theory and the Helmholtz principle
- Perform automatic lineament mapping, using the line segment detection algorithm
- Develop a validation method for the evaluation of the result

1.3.2 Research questions

- What are the optimal parameter values of the internal parameters of the algorithm for this application?

- What should be the geometrical representation of lineaments?
- Are the produced results plausible for the particular application?

1.4 RESEARCH APPROACH

The starting point of the adopted methodology is the Line Segment Detector (LSD) algorithm, developed by Grompone von Gioi et al. (2012). This LSD algorithm is based on Burns, Hanson and Riseman's method (Burns et al., 1986). It uses an *a contrario* validation model and detects meaningful alignments, based on the NFA.

This algorithm in C is provided by the authors in Grompone von Gioi et al. (2012). However, my intention is to develop the algorithm in R. The reasons behind this is that R is a well suited programming language for probabilistic and image processing computations. For a conversion step from C to R is, first, some modifications have to be done.

Further, a novel validation method is developed for the assessment of the quality of the results, based on a reference lineament map. The method introduces two error ratios, those of missing and false detections. These ratios are used for the tuning of the algorithm parameters and the accuracy assessment of the result.

1.5 THESIS STRUCTURE

Chapter 2 is a literature review on Gestalt theory for image processing, automatic lineament mapping and evaluation of automatically extracted features from images.

Chapter 3 presents the image and the reference data used in this research.

Chapter 4 describes all steps of the detection and validation methodology.

Chapter 5 presents the detection and validation results.

Chapter 6 introduces discussion points that were raised during all stages of the research.

Chapter 7 summarizes the conclusions and recommendations for future research.

Chapter 2

Literature review

2.1 GESTALT THEORY AND THE HELMHOLTZ PRINCIPLE

Gestalt theory is a branch of psychology which is one of the few that have attempted to describe the laws of human visual perception of images (Desolneux et al., 2008). It initiated by the definition of the gestalt laws by Max Wertheimer in 1923. Grouping laws is one of the main categories of Gestalt laws' list. These grouping laws define whether a set of points that share one or more similar characteristics, is perceived by a human as a coherent object, called gestalt (Desolneux et al., 2003a). In image analysis, these points are pixels of the image and the characteristic can be any property of the pixels, such as the colour or intensity.

The Helmholtz principle, along the same lines, asserts that no object is perceived in a random image (Desolneux et al., 2008). Therefore, it claims that only objects that deviate from randomness are perceived by humans. When a particular configuration of points with a common characteristic is observed, the Helmholtz principle examines whether this configuration is happening by chance or whether those points form indeed one object. For this validation, it is assumed that the particular feature of the points is randomly and uniformly distributed. That is called the *a-contrario* assumption (Desolneux et al., 2008). Under this assumption, from the tail of the binomial distribution it is inferred that the probability that at least k points out of a total number of n points share the same property is

$$B(n, k, p) = \sum_{i=k}^n \binom{n}{i} \cdot p^i \cdot (1-p)^{n-i} \quad (2.1)$$

where p is the probability that a point has the certain property (Desolneux et al., 2008). Suppose the examined property is the pixel intensity, which varies in the range $[0,255]$. If the intensity is assumed to be randomly and uniformly distributed, then the probability that a pixel has a particular intensity is $p = 1/256 = 0.004$. The probability that at least 10 over a total number of 100 pixels have a particular intensity value is $B(100, 10, 0.004) = 1.3 \cdot 10^{-11}$.

2.2 NUMBER OF FALSE ALARMS AND MEANINGFUL ALIGNMENTS

A particular point configuration is named an event and the event is called ε -meaningful if the expectation of its occurrence in random image is below a threshold ε (Desolneux et al., 2008). If the total number of potential point configurations is N , then the Number of False Alarms (NFA) of the event is defined as

$$\text{NFA} = N \cdot B(n, k, p). \quad (2.2)$$

The NFA is the probability of occurrence of this point configuration in a random image. The lower the NFA, the lower the probability in the white noise image and the more certain we can be

that the observed configuration is not a random event. The event is called ε -meaningful if $NFA < \varepsilon$ (Desolneux et al., 2008).

This concept is directly applicable to linear segments, where the quality of interest is the point orientation. In a segment of length l , that contains k points with the same orientation, the NFA associated with the segment is

$$NFA = N^4 \cdot \sum_{j=k}^l \binom{l}{j} \cdot p^j \cdot (1-p)^{l-j} \quad (2.3)$$

where N^4 is an approximation of the total number of possible segments in a $N \times N$ image (Desolneux et al., 2000).

2.3 RELATED WORK

Desolneux and co-workers have extensively studied the laws of Gestalt theory in image analysis. The mathematical framework of object detection on an image, without the need of any *a-priori* information is presented. It is applied for the detection of alignments and the notion of meaningful alignments is introduced. In (Desolneux et al., 2001) the use of the Helmholtz principle for object detection was described and two methods of edge and boundary detection were presented. Built upon the concept of meaningful segments, the notion of maximal meaningful segments in image analysis and its mathematical properties were discussed in (Desolneux et al., 2003b). Furthermore, the application of more grouping laws of Gestalt theory was demonstrated in (Desolneux et al., 2003a). Moreover, the same group of authors carried out a psychophysical experiment in order to examine whether the qualitative perception thresholds that are used in their method correspond to human perception. Finally, all the above work with more topics on Gestalt theory in image analysis are collected in Desolneux et al. (2008).

All the work of the aforementioned group of authors is applied in ordinary images. The single application, to our knowledge, of such an algorithm for a geo-information problem is the work of Michaelsen (2012) on automatic object extraction in aerial Near Infra-Red (NIR) images of urban terrain. In addition, Fallatah (2011) explored the applicability of the LSD algorithm (see next paragraph) for multi-spectral satellite images.

The Line Segment Detector (LSD) algorithm is a recent implementation of line segment detection based on the Helmholtz principle (Grompone von Gioi et al., 2012). It is based on the method of Burns et al. (1986) for the extraction of straight lines, which detects edges by grouping pixels with similar gradient orientation. It follows a line segment evaluation approach introduced by Desolneux et al. (2000), Desolneux et al. (2008), that assesses all detected segments. A Number of False Alarms is calculated for all the detected segments and the authors argue it works on any image without the need of parameter tuning. This is one of the issues of this research. The code is provided in C, in (Grompone von Gioi et al., 2012). This is the implementation on which the algorithm development of the current research is based.

2.4 AUTOMATIC LINEAMENT MAPPING

First attempts for automatic mapping of geological lineaments include the use of the Hough transform (Wang and Howarth, 1990), implementation of a Segment Tracing Algorithm (STA) for automatic detection on LANDSAT TM images (Koike et al., 1995) and an approach to combine the use of digital elevation models with second derivative filters (Wladis, 1999). Later, Mavrantza and Argialas (2002) compared the performance of various edge detection algorithms and operators, including Laplacian, Sobel and Kirsch operators, for LANDSAT 7 TM images. In Mavrantza and

Argialas (2008) an object-oriented image analysis approach for geological lineament identification was presented. In more recent work (Marghany and Hashim, 2010; Marghany et al., 2009) the Canny algorithm has been applied for automatic mapping from LANDSAT images and 3D image reconstruction in combination with SRTM data.

2.5 EVALUATION OF AUTOMATICALLY EXTRACTED FEATURES

Validation methods of automatically extracted geological lineaments are not encountered in literature. However, there are several methods presented in the broader framework of automatically extracted features from images. There is abundant literature on the evaluation of automatically extracted roads (Péteri et al., 2004; Song et al., 2001). Heipke et al. (1997) explore ways to describe the level of correspondence between automatically extracted road networks and a reference dataset. They describe a set of quality measures, where correctness and completeness are the two prominent ones. Evaluation consists of two steps, one to find matching features between reference and extraction, followed by measure calculation. Both extracted and reference lines are first grown by a buffer and then the length of the extracted or reference lines that fall inside the buffer zone and the total length of the extracted lines is measured. The same measures have been used by Song et al. (2001) for automatic road extraction evaluation, and in addition for building extraction as well as classification accuracy assessment by McKeown et al. (2000). The same set of quality measures have been applied twice for the evaluation of the LSD detection results and the exploration of the effect of parameter values on the detection result. Mwakisunga (2010) assessed the quality of the LSD detection result on a LANDSAT 7 ETM image of agricultural fields. Fallatah (2011) validated the detection result from a Geo-Eye-1 image of urban area.

In a more general and not application specific approach, Goodchild and Jeansoulin (1998) describe a new method for the comparison of two sets of lines. They suggest that for each point in a line A we can define its closest Euclidean distance to a line B and obtain a measure of relative accuracy between them. The same applies in the other direction, from line B to line A. Those distance functions can then be represented in a histogram (Goodchild and Jeansoulin, 1998).

Chapter 3

Data

This chapter locates the study area of this project. It describes the imagery used for the study and the vector reference data used for the validation of the result.

3.1 STUDY AREA

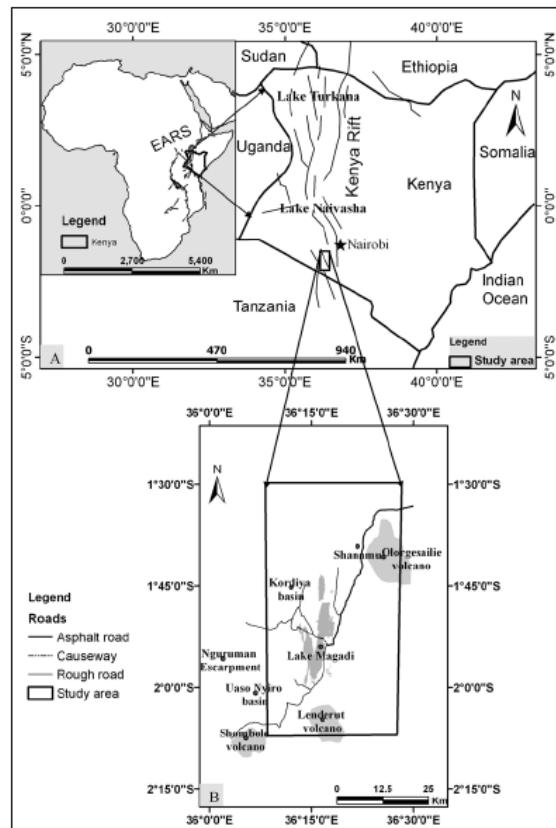


Figure 3.1: Location of the African Rift in Kenya, with major fault traces (top). Lake Magadi region (bottom), reprinted from Sequar (2009).

The region considered for this study is part of the southern Kenyan Rift, situated north of lake Magadi in Kenya (Figure 3.1). It is part of the East African Rift System (EARS), that extends from the Red Sea down to Mozambique (Kuria, 2011). The Kenyan rift is regarded as one of the first occurrences of tectonic activity in the continent (Achauer and Masson, 2002). In particular, the Magadi area is a region where rifting is still observed.

Table 3.1 Spectral range of ASTER VNIR bands (ERSDAC (2005))

	Band no	Spectral range (μm)
VNIR	1	0.52 - 0.60
	2	0.63 - 0.69
	3N	0.78 - 0.86

3.2 IMAGES

The image used for the study is an ASTER scene of the Magadi area, acquired in 2007. The area covered by the scene is approximately 4000 km². For this study, the three bands in the visible near-infrared (VNIR) spectrum were used, since those are the ones usually exploited for geological interpretation. The spectral range of each band is presented in Table 3.1. The spatial resolution of all VNIR bands is 15 m. The coordinate system is the Universal Transverse Mercator (UTM), Zone 37 South, and the datum World Geodetic System (WGS) 1984. The image is a Level B1 ASTER product. Level 1B products are radiometrically calibrated and geometrically co-registered data for all image bands (ERSDAC, 2005).

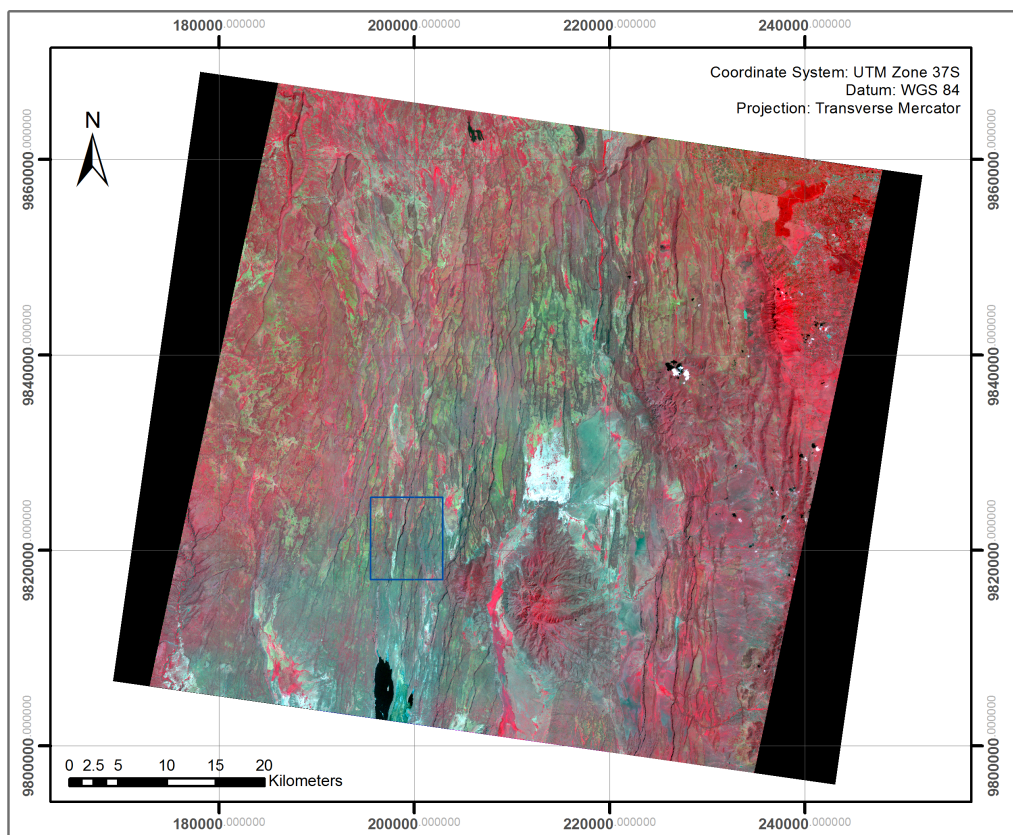


Figure 3.2: ASTER Image AST-L1B-00301232007080046-20131023124004-21811. The area marked as blue was selected as a test area for parameter tuning.

Due to demanding computations, a subset of the scene was used for the parameter tuning. The subset has an extent of 61 km² and is indicated in Figure 3.2. The subset was selected such that it is representative of the surrounding area and contains most of the characteristic lineament forms

that exist in the region. Major and long lineaments, as well as minor ones are encountered over the subset.

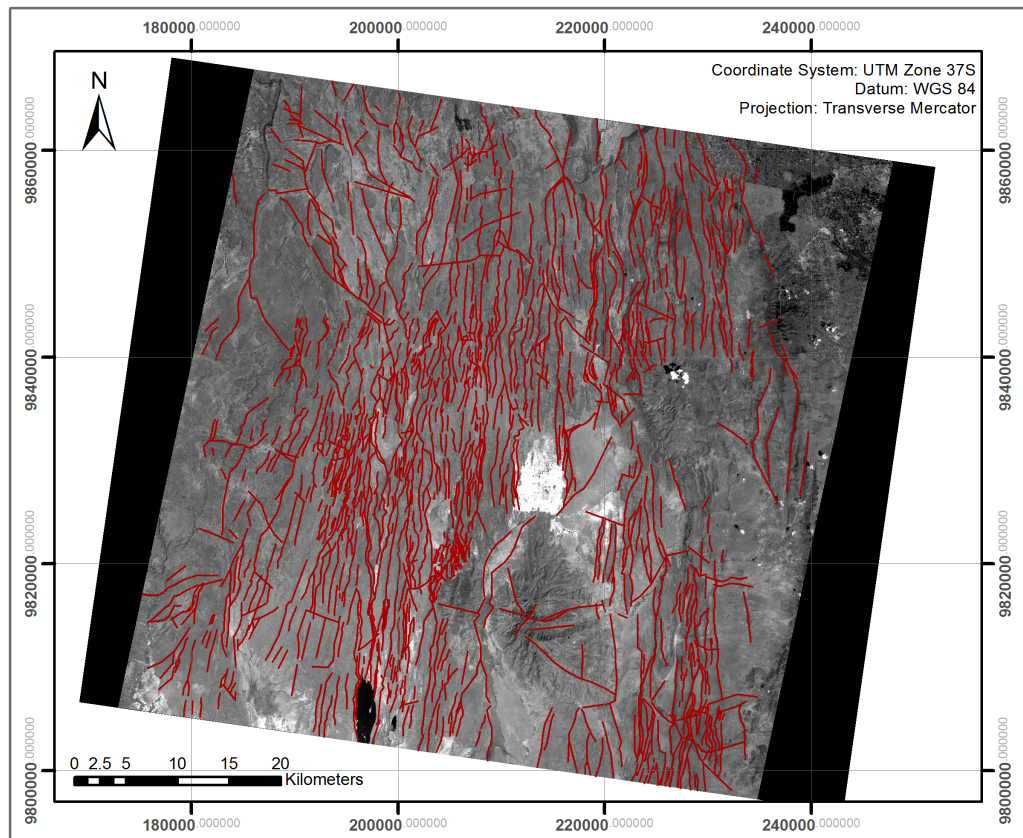


Figure 3.3: Reference lineament map, draped over Band 1 of ASTER image

3.3 REFERENCE DATA

The reference data is a vector lineament map (Figure 3.3). It is a product of manual interpretation (Woldai, October 2013), over the whole scene. The respective parts of the dataset were used for tuning and validation. The rose diagram of the reference data depicts one main direction N-NNE/S-SSW, with some lineaments in a NW/SE (Figure 3.4).

Figure 3.5 illustrates the interpretation process of the lineament position on two characteristic structures of the study area, a graben (3.5a) and a horst (3.5b). The position of the lineament is indicated in green. The delineation of the lineament is often obstructed by shadow. If the sun is at such an angle that it faces the scarp (Figure 3.5a) then the lineament is clearly visible and can be delineated. In the opposite case, the shadow of the fault scarp covers the position where the crusting is happening. In those cases, the delineation is performed on the opposite edge of the fault plane, indicated in blue in Figure 3.5. Since this study did not include identification of the lineaments in order to determine whether those are faults or other rift structures, the term lineament will be used throughout.

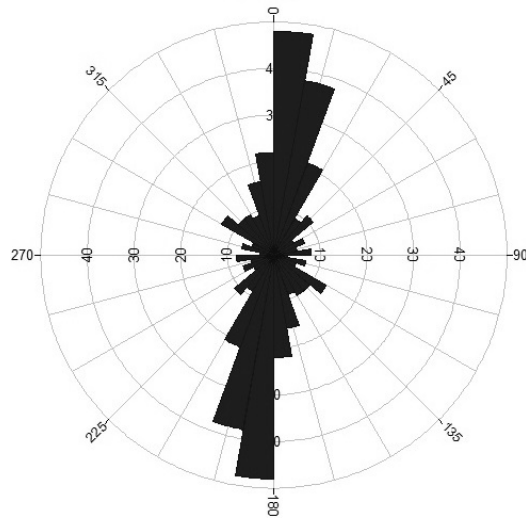


Figure 3.4: Rose diagram of the lineaments in the reference dataset

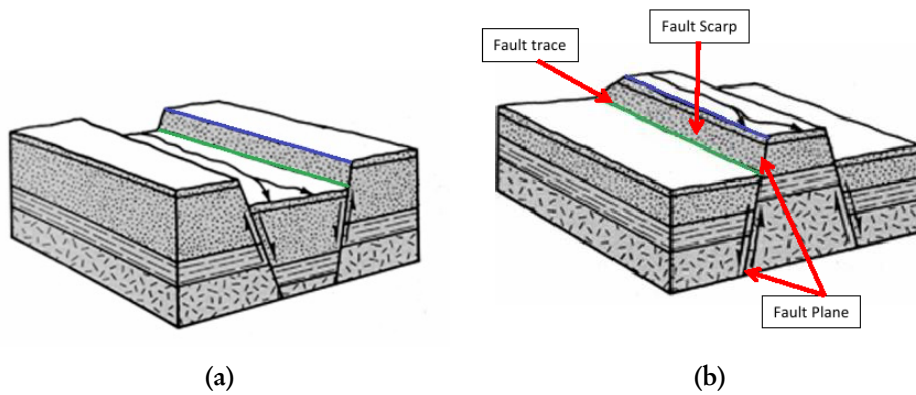


Figure 3.5: Illustration of fault trace, scarp and plane. Green lines indicate the lineament (possibly a fault), where the crusting is happening. When the lineament is obstructed by shadow the delineation is carried out on the opposite edge of the scarp, indicated in blue. (a) Graben structure, (b) Horst structure (Illustration from Woldai (October 2013), background image reprinted from E.R.S. (2014))

Chapter 4

Method

4.1 SEGMENT DETECTION ALGORITHM

The presented algorithm is a line segment detection algorithm based on pixel gradient. It initiates by calculating a *level-line angle* for every pixel (Section 4.1.3). This angle stems from the gradient of the pixel and depicts the direction of the edge that is encountered in each position. These angles are used to form regions that consist of neighbouring pixels with similar *level-line angles*, which are called *line-support regions* (Section 4.1.5). Each *line-support region* is a candidate for a segment. Every region is validated against an *a contrario* model. This model is an image where gradient angles are randomly and uniformly distributed around the image. The validation is based on the calculation of a Number of False Alarms (NFA), which shows the probability that a particular event (*line-support region*) would occur in the *a contrario* model (Section 4.1.7). If this probability is low, then the segment is validated as meaningful and, therefore, considered a true detection.

The algorithm has a number of internal parameters involved in some of its parts. Their values are not discussed in this section. The selection of their values was based on a novel tuning method that was developed and is presented in section 4.2.

4.1.1 Multispectral data

The segment detection algorithm takes as input a single band (grey-scale) image. However, Remote Sensing commonly involves multi-spectral data. The image data used in this research is an ASTER image. Using only one of the available bands it means that spectral information contained in other bands is ignored and does not contribute in the result. In order to concentrate all the available spectral information in a single band, Principal Components Analysis (PCA) is performed on the image. If $k < n$, PCA is a linear transformation of an n -dimensional vector into a k -dimensional vector with minimum correlation between its components (Du and Swamy, 2014). The spectral bands that are commonly used for the task of geological interpretation and lineament mapping are the ones in the visible spectrum (Woldai, October 2013). Hence, the PCA was performed on the three ASTER bands of the visible and near-infrared spectrum. The first component was selected because it explained the maximum variability of the data.

4.1.2 Image scaling

The first step of the process is a rescaling of the image to a lower spatial resolution, with a scale factor S . There are two reasons for this. The first is to tackle problems of aliasing and quantization artefacts (Grompone von Gioi et al., 2012). Secondly, it is important to rescale the image in such a scale that facilitates the automatic extraction of features of interest. The optimal value of this scale factor is one of the research questions this research intends to answer.

Image sub-sampling is performed in two steps. First, a Gaussian filter is applied for smoothing, in order to avoid aliasing (Grompone von Gioi et al., 2012). The kernel size is 5×5 and the standard

deviation $\sigma = 0.8/S$. These two values were selected via a series of trials and visual inspection of the result. After the filtering, the sub-sampling is performed on the smoothed image.

4.1.3 Gradient computation

\dots	\vdots	\vdots	\dots
\dots	$i(x, y)$	$i(x + 1, y)$	\dots
\dots	$i(x, y + 1)$	$i(x + 1, y + 1)$	\dots
\dots	\vdots	\vdots	\dots

Figure 4.1: Gradient calculation mask, reprinted from Grompone von Gioi et al. (2012)

The gradient computation considers a 2×2 neighbourhood (Figure 4.1).

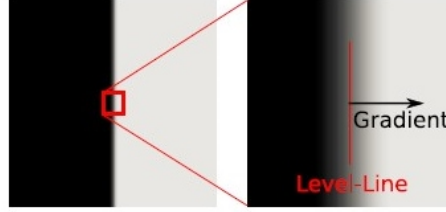


Figure 4.2: Level-line angle. It is zero for perfectly horizontal edges, here $\phi = 90^\circ$. It depicts the direction of the edge, reprinted from Grompone von Gioi et al. (2012)

If $i(x, y)$ is the gray level value at (x, y) , the pixel gradient at (x, y) is calculated as

$$g_x(x, y) = \frac{i(x + 1, y) + i(x + 1, y + 1) - i(x, y) - i(x, y + 1)}{2} \quad (4.1)$$

$$g_y(x, y) = \frac{i(x, y + 1) + i(x + 1, y + 1) - i(x, y) - i(x + 1, y)}{2} \quad (4.2)$$

The gradient magnitude is

$$G(x, y) = \sqrt{g_x^2(x, y) + g_y^2(x, y)}. \quad (4.3)$$

The gradients in two directions (g_x and g_y) are also used to calculate the *level-line angle* (Figure 4.3b)

$$\phi_i = \arctan\left(\frac{g_x}{-g_y}\right) \quad (4.4)$$

(Grompone von Gioi et al., 2012). The level-line angle is perpendicular to the gradient direction and describes the direction of the edge (Figure 4.2).

The size of the used mask is the smallest possible, so that the dependence between the resulting gradient values is minimum and the assumption that the image gradient is randomly and uniformly distributed is not rebutted. In theory, in a noisy image, there is no dependence between the values of the pixels.

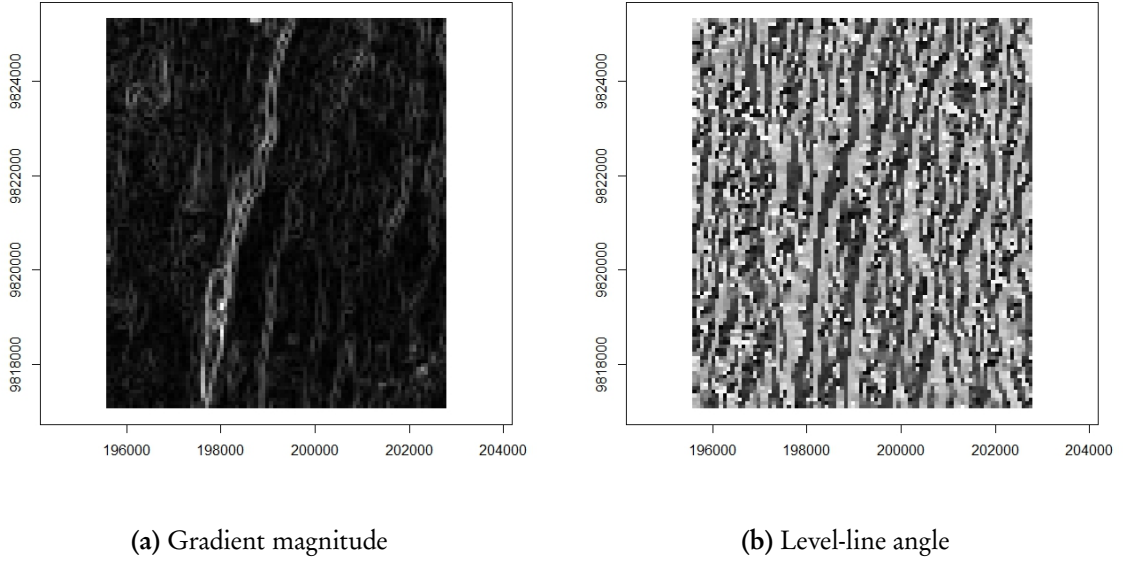


Figure 4.3: Gradient Images

4.1.4 Gradient ordering and threshold

The formation of line-support regions of potential segments (Section 4.1.5) is based on the *level-line angles* of the pixels. Starting from one seed pixel, the region is grown by adding more pixels with similar angles. It is expected that pixels with high gradient magnitudes are pixels that lie on edges. Therefore, it is reasonable to use pixels with large magnitudes as seed pixels for the region growing process. For this reason, pixels are ordered descending, on the basis of their gradient magnitude. This list is the one from which seed pixels are drawn consecutively.

The higher the gradient magnitude, the more likely it is that the pixel is member of an edge on the image. Pixels with very low magnitudes, on the other hand, represent flat zones or smooth transitions. For this reason, pixels with low gradient magnitude are rejected and not used in the formation of line support regions. Hence, according to Grompone von Gioi et al. (2012), a threshold is applied to the magnitude:

$$\rho = \frac{q}{\sin \tau}. \quad (4.5)$$

The parameter q is related to the possible error of the gradient, due to quantization effects and is set equal to 2. The parameter τ is the angle tolerance used in region growing (Section 4.1.5). From Equation 4.5 it is inferred that the gradient magnitude threshold is inversely proportional to $\sin \tau$. The idea behind this relationship is that pixels whose angle error is larger than the angle tolerance should be rejected.

4.1.5 Region growing

The region growing algorithm, takes as input iteratively a seed pixel and its *level-line angle*, looks for neighbouring pixels with similar angles and groups them together. Starting from the first pixel in the sorted list of gradient magnitudes, the algorithm is looking for neighbouring pixels whose level-line angle is equal to the angle of the region, up to a tolerance τ . These pixels will form the line support region of the potential segment. Each pixel can only be member of a single line-support

region (Figure 4.4).

For the growing, an 8-connected neighbourhood system is used. The initial *region angle* θ_{region} is

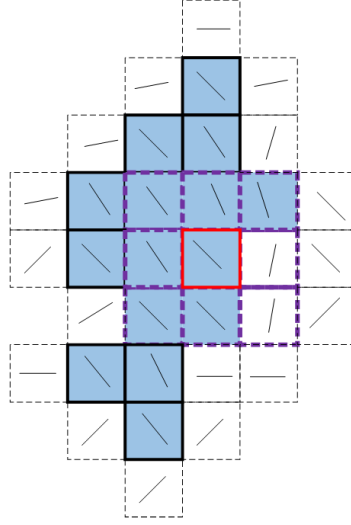


Figure 4.4: Example of a *line-support region*, neighbouring pixels with similar *level-line angles* get grouped together. The algorithm is using an 8-connected neighbourhood system.

the *level-line angle* of the seed pixel. Each time a pixel is added to the region the region angle is updated as follows

$$\theta_{region} = \arctan \left(\frac{\sum_j \sin \phi_j}{\sum_j \cos \phi_j} \right) \quad (4.6)$$

where ϕ_j is the *level line angle* of the added point. The process terminates when no other pixel can be subjoined to the region.

The result of the region growing algorithm is a set of segments, that are composed of pixels with similar level-line angles and whose magnitudes are above the magnitude threshold. Each one of these segments is a line segment candidate with an associated region angle.

Before proceeding, regions with no more than two pixels are deleted.

4.1.6 Rectangle approximation

Line-support regions are structures that need to be approximated by a geometrical event, in order to be evaluated as meaningful or not. Here *line-support regions* are approximated by rectangles, which is a shape that resembles the appearance of a line segment on an image, considering a relatively small width.

Each pixel is assigned a weight proportional its gradient magnitude and that is called the “mass” of the pixel. Then, the centre of the rectangle is the mass centre of the region and the rectangle direction is the first inertia axis of the region. The mass centre (c_x, c_y) is calculated as follows:

$$c_x = \frac{\sum_{j \in region} G(j) \cdot x(j)}{\sum_{j \in region} G(j)} \quad (4.7)$$

$$c_y = \frac{\sum_{j \in region} G(j) \cdot y(j)}{\sum_{j \in region} G(j)} \quad (4.8)$$

where $G(j)$ is the gradient magnitude of the pixel $j \in region$ and j runs over all region pixels. The rectangle direction is, in reality, defined after a Principal Components Analysis (PCA) on

the gradient magnitudes of the region pixels. The direction coincides with the direction of the minimum variance of gradient magnitudes (Figure 4.5).

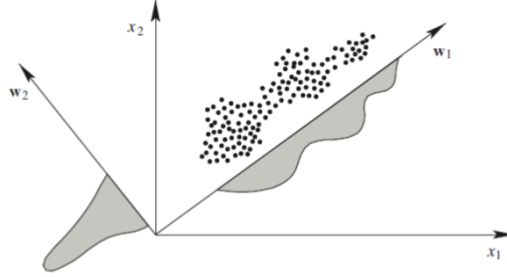


Figure 4.5: PCA transformation, reprinted from Du and Swamy (2014)

This direction is the eigenvector angle linked to the smallest eigenvalue of the matrix

$$M = \begin{pmatrix} m_{xx} & m_{xy} \\ m_{xy} & m_{yy} \end{pmatrix}$$

where

$$m_{xx} = \frac{\sum_{j \in Region} G(j) \cdot (x(j) - c_x)^2}{\sum_{j \in Region} G(j)} \quad (4.9)$$

$$m_{yy} = \frac{\sum_{j \in Region} G(j) \cdot (y(j) - c_y)^2}{\sum_{j \in Region} G(j)} \quad (4.10)$$

$$m_{xy} = \frac{\sum_{j \in Region} G(j) \cdot (x(j) - c_x) \cdot (y(j) - c_y)}{\sum_{j \in Region} G(j)} \quad (4.11)$$

Finally, the resulting object is the minimum rectangle that contains all the pixels of the *line-support region* (Figure 4.6).

4.1.7 Number of False Alarms (NFA) calculation

For the validation of the detected segments an *a contrario* model is used. That is, it is assumed that the observations, the gradient angles, are realizations of a uniformly distributed variable. Then, a configuration of pixels with an associated quality (gradient angle) is specified. In our case, this is a group of neighbouring pixels that have similar level line angles, a *line-support region*. For this particular configuration, its probability of occurrence in the *a contrario* model, that of white noise, can be calculated. The lower this probability, the more certain it is that our configuration represents an actual object in the image and that the detection is not an artefact of noise. The probability of occurrence is directly related to the NFA, which is calculated considering how many of the pixels that form a potential segment are aligned, given a precision p (Figure 4.6). The NFA calculation is based on the binomial tail, over the random uniform distribution.

In order to decide whether a segment is significant, this probability is bounded by a value ε . The lower the value of ε , the stricter we are with defining “meaningfulness” (Figure 4.7). Hence, only segments that would very hardly occur in a random image are accepted. The ε variable is strongly related to the concept of significance level in statistics and, therefore, usually it is set to values

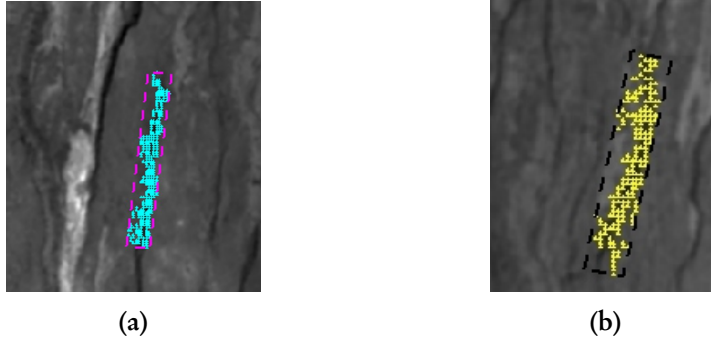


Figure 4.6: Examples of associated rectangles: the minimum rectangle that contains all the pixels of the *line-support region*. (a) High density of aligned points, low NFA. (b) Lower density of aligned points, higher NFA. Pixels in color are aligned points of the region.

$\varepsilon \ll 1$ (Desolneux et al., 2000). Here, the null hypothesis is a random distribution of the image gradient. Based on a choice of significance level, the null hypothesis is rejected when the probability (NFA) of a particular object is lower than this significance level.

The NFA calculation considers three values:

- total number of aligned points in the rectangle (k)
- total number of pixels in the rectangle (n)
- precision (p)

The precision p is the probability that a pixel has a certain orientation in the *a contrario* model and is set to $p = \tau/\pi$ (Grompone von Gioi et al., 2012). Clearly, this value is related to the angle tolerance τ and the precision with which angles are considered.

The NFA associated with a rectangle is

$$\text{NFA}(r) = (N \cdot M)^{\frac{5}{2}} \cdot \gamma \cdot B(n, k, p) \quad (4.12)$$

$$B(n, k, p) = \sum_{j=k}^n \binom{n}{j} \cdot p^j \cdot (1-p)^{n-j} \quad (4.13)$$

where N and M are the image dimensions and $(N \cdot M)^{\frac{5}{2}}$ the total number of rectangles considered on the image (Grompone von Gioi et al., 2012). The parameter γ is the total number of p values tested. Here, only the value $p = \tau/\pi$ was used, hence $\gamma = 1$.

The NFA is then bounded by the threshold ε and only the rectangles for which $\text{NFA}(r) < \varepsilon$ are validated as ε -meaningful segments. The value of the parameter ε is among the ones that are examined in the tuning process (Section 4.2).

4.2 PARAMETER TUNING AND VALIDATION

In this section, the validation method developed for parameter tuning is presented. The method is applied firstly to calibrate the internal parameters of the algorithm. Secondly, once the parameters are fixed, the method can be used to evaluate the result obtained from any subset in terms of missing and false detections. In addition, a measure of the positional accuracy of the successful detections is provided.

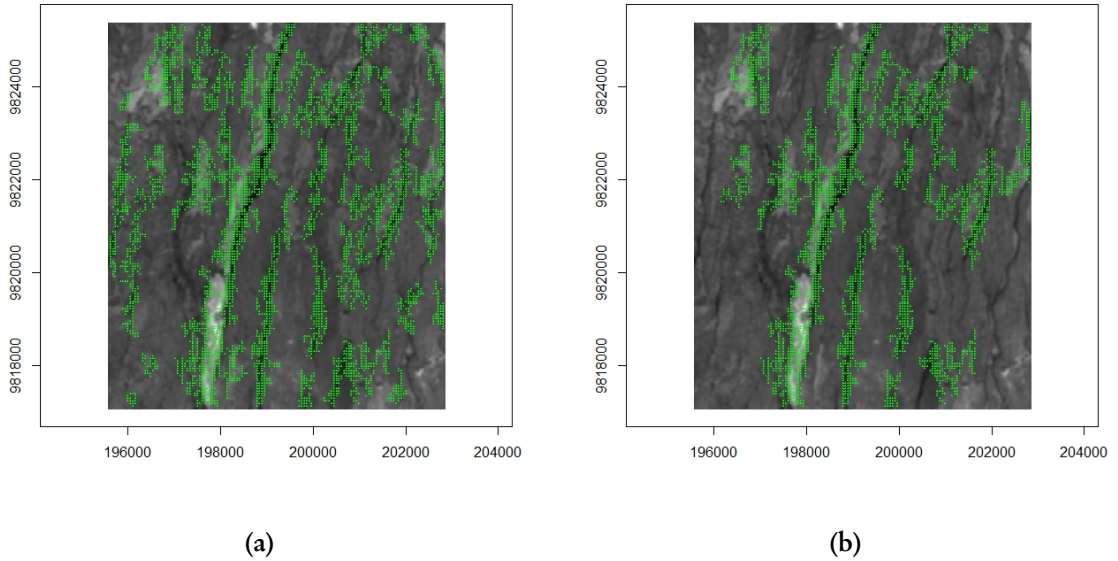


Figure 4.7: Meaningful Segments for different values of ε . (a) Meaningful segments for $\varepsilon = 1$, (b) Meaningful segments for $\varepsilon = 10^{-10}$. Small ε values imply stricter threshold to the NFA. As a result, fewer segments are accepted as meaningful, those with very low probability of occurrence in the white noise image model.

Parameter tuning is performed on a small subset of the study area, due to large computational requirements. The algorithm parameters that are tuned are the scale factor S , the angle tolerance τ and the NFA threshold ε .

The present method is a novel scheme for the assessment of the relative positional accuracy between a reference dataset of linear features and an automatic extraction of the respective features. It is based on the method of Goodchild and Jeansoulin (1998) for the comparison of two sets of lines. As a measure of similarity between two sets of lines they suggest that for each point in a line A we can define its shortest Euclidean distance to a line B and obtain a measure of relative accuracy between them. The same applies in the other direction, from line B to line A . Those distance functions can then be represented in a histogram. This approach was adjusted to the geometrical characteristics of our result. Comparison in this case has to be applied between a set of lines (reference) and a set of points (extraction). The extraction result of the detection algorithm is a set of meaningful segments, which consist of a number of pixels. In addition, the method is extended and apart from distance measures between reference and extraction, considers also differences in local orientations.

This method exploits the distance and difference in orientation between a reference and an extracted dataset to assess the level of correspondence and similarity among them. The distinctiveness of the method is that it handles two datasets that represent the same feature (lineaments) under a different geometrical type; lines from the reference dataset and points from the extraction. The approach establishes measures between sample points on the lines and the detected points.

4.2.1 Interval points on reference lines

For the reference lines, sampling points are selected on equal distances along their total extent. The sampling distance is set equal to $2 \times R$, where R is the pixel size. R depends on the scale factor S and is equal to $R = r/S$, where r is the original pixel size $r = 15$ m. Pixels are square.

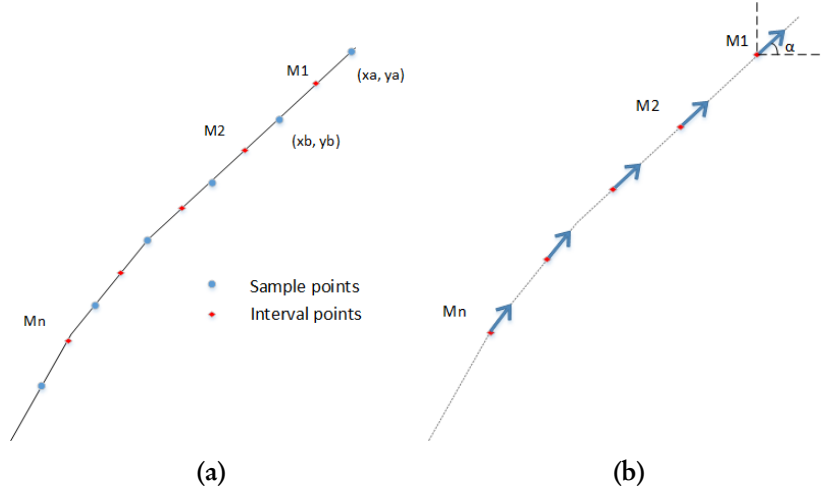


Figure 4.8: Interval points and local orientation. (a) Sample and interval points on a reference line, (b) Local orientation at interval points

Sample points are located on equal intervals on all lines. In between each pair of sample points an interval point M_i is defined, in the middle of the distance of the sample points (Figure 4.8a). Such short segments can be considered as straight line segments and, hence the coordinates and local orientation of the interval points are

$$x_{M_i} = \frac{x_i + x_{i+1}}{2}, y_{M_i} = \frac{y_i + y_{i+1}}{2} \quad (4.14)$$

$$\alpha_i = \arctan \frac{y_{i+1} - y_i}{x_{i+1} - x_i} \quad (4.15)$$

where x_i, y_i are the coordinates of the sample points.

4.2.2 Local orientation of detected points

Each one of the detected points belongs to a single segment which has an orientation, the global *level-line angle* of the segment. This angle is calculated as

$$\theta_{region} = \arctan \frac{\sum_{j \in region} \sin \phi_j}{\sum_{j \in region} \cos \phi_j} \quad (4.16)$$

where ϕ_j is the *level-line angle* and j a running index on all region pixels.

From the equation above we see that all points participate equally to this global measure of orientation of the segment. However, since the detected segments are not perfectly straight lines, but rather slightly curvilinear features we are more interested in a local orientation measure at each segment point (Figure 4.10). In order to achieve this, the local angle computation assigns to all region points weights proportional to the distance from the point in question (Hastie et al., 2009). Here, a Gaussian kernel is used and the local angle calculation is as follows

$$\theta_l = \arctan \frac{\sum_{i=1}^k e^{(-d_i/d_0)^2} \cdot \sin \phi_i}{\sum_{i=1}^k e^{(-d_i/d_0)^2} \cdot \cos \phi_i} \quad (4.17)$$

where d_i is the distance of the pixel i from the pixel l at which the local orientation is calculated, d_0 controls the weights assigned to the pixels and $k = k_s^2$, where k_s is the kernel size.

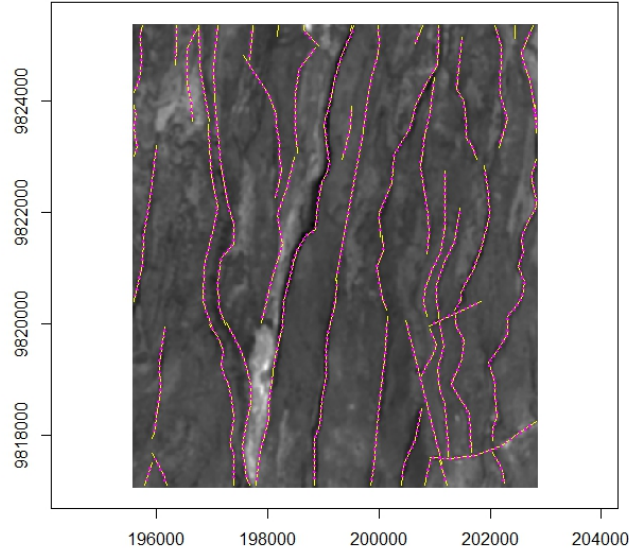


Figure 4.9: Reference lines and interval points. Reference lines are plotted in yellow and interval points, at intervals of two pixels are shown in red.

4.2.3 Distance measures and accuracy assessment

Once local orientations are calculated, corresponding points between reference and detection are sought. A pair of points is considered a correspondence when the two points are close and share similar local orientations. The same measures are applied both starting from reference and detected points respectively. The conditions for two points to be considered corresponding are:

$$S < d_{r,e} \quad (4.18)$$

$$|\alpha - \theta_l| < \theta_0 \quad (4.19)$$

where S is the distance between the two points, d_r and d_e two distance thresholds and θ_0 the angle threshold.

The condition on the local angles prevents from finding false correspondences between points that are very close, but belong to objects with distinct orientations (Figure 4.10b).

From reference to detection

If a corresponding point is found for the interval point of the reference line, then this is counted as a successful detection. If such point does not exist, then it is counted as a missing one. The following ratios of missing (N_M) and successful (N_{S_r}) detections are defined:

$$N_M = \frac{\text{total number of interval points with no correspondence}}{\text{total number of interval points}} \quad (4.20)$$

$$N_{S_r} = 1 - N_M \quad (4.21)$$

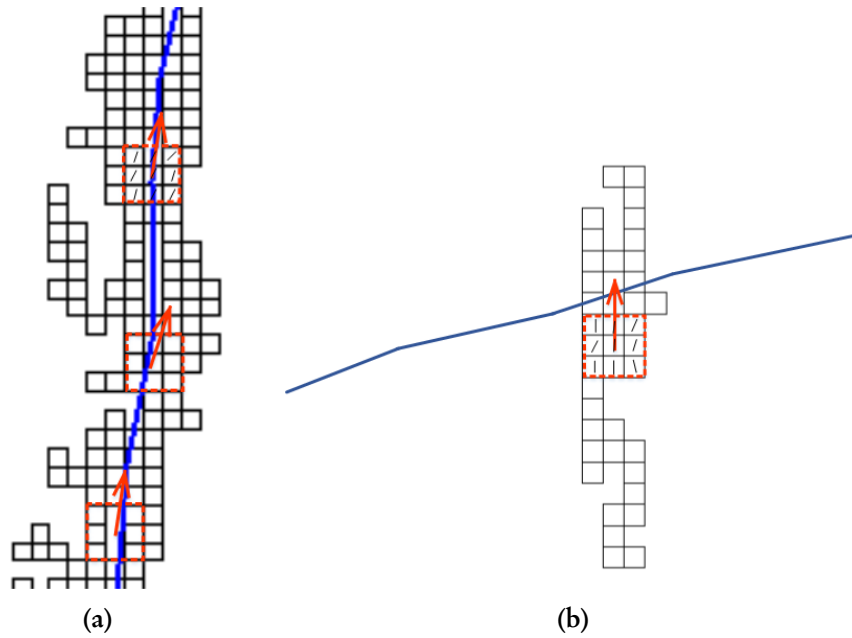


Figure 4.10: Local angle calculation of detected points. The local computation makes use of a 3×3 kernel (red). Example *level-line angles* are shown with black segments inside the pixels. (a) Similar segment and line orientations. There is correspondence among the local orientation of the line and segment points. (b) Different segment and line orientations. The method will not indicate a corresponding pair of line and segment point, due to difference in local orientations, despite the intersection.

Here, the percentage of successful and missing detections is a measure of completeness of the result, with respect to the reference. High N_{S_r} values would imply that the line intersects with many detected points that are also aligned.

From detection to reference

The same procedure is repeated from the detected points to the interval points of the reference lines. If a corresponding interval point is found for the extracted point, then the detection is considered successful. If not, then this extracted point is a false detection. The respective ratios of false (N_F) and successful (N_{S_e}) detections will now be:

$$N_F = \frac{\text{total number of detected points with no correspondence}}{\text{total number of detected points}} \quad (4.22)$$

$$N_{S_e} = 1 - N_F \quad (4.23)$$

In this case, the correctness of the result is assessed. False detections represent false positives and successful detections are true positives. High N_F ratios imply that either the detected points are mispositioned, in relation to the lines, or that they don't have similar orientations.

Accuracy assessment

Once the successful detections are assorted, then they can be used in order to examine the positional accuracy of the result. For this purpose, the mean and the standard deviation of the distances

of corresponding points are calculated for all successful detections. These values express the deviation between reference and detection, in terms of distance.

4.2.4 Implementation

The validation method involves a number of additional parameters. First, distance thresholds distinguish the detections that have passed the NFA control into successful and unsuccessful and counts false and missing detections. Second, the angle threshold (θ_0) that defines when an extracted and a point on the reference line are aligned, based on their local orientations. Finally, the size and the standard deviation of the Gaussian kernel, used as an averaging tool for the local angle calculation of the segment points.

The distance threshold should be different for the distance measures from the reference to the extraction (d_r) and from the extraction to the reference (d_e) (Eq. 4.18). The reason is the nature of the objects to be compared. The sample reference points are points that lie on lines, those of geological interpretation. The extracted points are those of the segments formed during region growing. As it has been observed from the results these segments are objects that cover an area, rather than strict linear objects. An example of such a comparison between a reference and a detected object is shown in Figure 4.11. Starting from a point on the line to find the closest aligned point in the set of extracted points, it is expected and required to find one within one to two pixels, in order to consider that the particular sample point has been detected. When starting from the segment points, we are dealing with points all over the area of the segment. For the points on the edges of the segment the resulting distances can be larger than two pixels although they have correctly been assigned to the segment, which in the image appears as a wide object rather than a line. Therefore, there is a need to set a higher distance threshold for the calculation that starts from the extraction and moves towards the reference points.

The distance threshold from reference to detection (d_r) (Eq. 4.18) is linked to the relative positional accuracy of the detected segments and the reference lines. For this distance a deviation of 1-2 pixels is acceptable (Woldai, October 2013) and, hence, the threshold was set equal to two pixels. Therefore, it is different for every value of S . The resulting distance threshold values for every S value are reported in Table 5.1. Once the scale factor is fixed, the distance threshold d_r is fixed as well.

The distance threshold from detection to reference is related to the width of the detected segments, which is different for every S . For this study, the distance threshold from extraction to reference (d_e) is set equal to the first quantile of the width of the detected segments (in practice, this width is approximated by the width of the associated rectangles of the segments). Table 5.1 shows that this threshold value is different for coarse and fine scales. This is explained by the nature of the segments that are formed. The region growing method applied here is a pixel-based method and, hence, the shape and size of the resulting segments is very much scale dependent. It is observed that the coarser the scale, the wider the final objects. It is also expected that the detection precision cannot be equally small in coarse and fine resolutions.

The angle threshold (θ_0) is related to the precision with which the lineament orientation is detected. Moreover, it strongly connects to the question: “When can we say that two lineaments share the same orientation?”.

Frequently, lineament orientations are classified in intervals of 10° (Singhal and Gupta, 2010). Here an additional error in the orientation estimation due to image smoothing was considered and the angle threshold was set to 12.5° (Eq. 4.19).

For the Gaussian kernel, the size is $k_s = 3$ (3×3), since the average width of the segments is not much larger than this length. Also, the standard deviation of the exponential function (d_0) is chosen to be equal to the first quantile of the segments’ length divided by the pixel size (again the

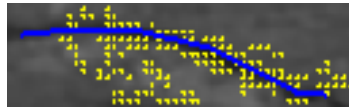


Figure 4.11: Example of a detected segment and its corresponding reference line. The distance of the points of the core of the segment from the line is very small. The distance of the points along the segment edges from the line is larger, although the segment they belong to has a clear correspondence to the reference. Image is rotated.

segment length is approximated by the rectangle's main axis length). This parameter is associated with the window size of the kernel (Hastie et al., 2009).

4.3 ASSESSMENT OF THE DETECTED SEGMENTS

This section presents a simple method of describing the nature of the detected segments and their relationship with the reference lineaments. It is based on the intersection of the segment with its corresponding reference lineament. The assumption that the lineaments have a N-S orientation is made for simplification reasons. This assumption does not deviate much from reality since the main direction of lineaments in the area is N-NNE/S-SSW (Figure 3.4). The assumption is not restrictive, since the method can be easily adjusted for different lineament orientations.

On each line, sample points at interval of one pixel are drawn. Sample points that intersect with a segment are called *hits* (Figure 4.12). When a *hit* is found then the number of segment points that lie on a horizontal line crossing the hit point are counted, both on the left and right side. The horizontal line is used based on the N-S direction assumption. The ratio of the sum of distances of points lying on the two sides of the line is calculated. Further, the mean distance of the hit points from the detected points that have been counted is computed, along with the standard deviation. Finally, the ratio of hits over the total number of sample points on the line is recorded.

The goal of this analysis is to provide a detailed insight in the geometrical relationship between reference lineaments and automatically detected segments. The analysis was applied on a single segment.

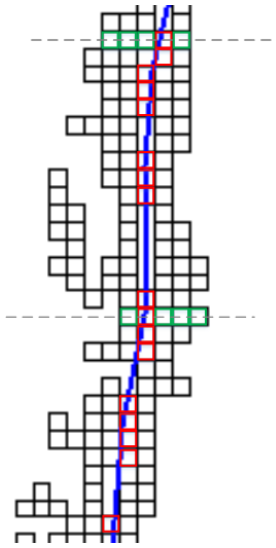


Figure 4.12: Points of intersection of the reference lineament with its corresponding detected segment. Intersection points are called *bits* (red). The points lying on the respective horizontal line are counted (green).

Chapter 5

Results

5.1 INTRODUCTION

In this section the tuning results for the three internal algorithm parameters are presented. Those parameters are the scale factor (S), the angle tolerance (τ) and the Number of False Alarms (NFA) threshold (ε). Each parameter is estimated individually. In all cases, tuning is performed by varying the value of the parameter in question, while the other two are fixed. Tuning runs over a line parallel to the parameter that is being tuned, in 2D space (Figure 5.1b). The final goal is to spot the point in 3D space, where each parameter has its optimal value (Figure 5.1a).

The sequence in which the parameters are tuned is based on their order of appearance in the algorithm but also their influence. The first parameter to be tuned is the scale factor S . Image sub-sampling precedes all other algorithm steps. Consequently, the resulting spatial resolution of the sub-sampling has an impact on the smoothing that follows. In addition, during region growing, the total number of pixels that form a line support region is directly related to the spatial resolution. The coarser the resolution, the smaller the number of pixels per region will become. Therefore, the scale parameter is fixed first.

Following is the angle tolerance parameter. This parameter is determinant in the region growing algorithm, which runs over the sub-sampled image. The angle tolerance influences the final shape and size (in pixels) of the *line-support-regions*, which in turn will be evaluated with the calculation of NFA.

NFA calculation and the selection of meaningful segments happens last. The distinction between true detections and false alarms is controlled by the parameter ε .

5.2 TUNING OF SCALE PARAMETER

Values in the range $[0.1, 1]$ at intervals of 0.1 were tested. If an abrupt change was noticed between two consecutive values in the missing or the false detections' ratios, additional S values were tested, in order to obtain a clear description of the trend in the errors. For this reason, tests for the values 0.05, 0.125 and 0.15 were added. The results are presented in Table 5.1. Low S implies coarse, while high S fine spatial resolution.

The fixed parameters of the other two values were $\tau = 20^\circ$ and $\varepsilon = 1$, which seem to be close to the optimal from visual inspection of multiple test results.

An illustration of the trend of false (N_F) and missing (N_M) detections for varying scale factors is presented in Figure 5.2a. In the tested range of scale factor values, N_F shows a larger variation than N_M . The first varies from values of 0.02 to 0.72, whereas N_M is limited in the value range $[0.38, 0.55]$. On the function of missing detections, a minimum is observed for $S=0.2$ and $S=0.3$, where the ratio values are equal. For $S<0.2$, the ratio of missing detections follows an increasing pattern. The same happens for $S>0.3$. The maximum value of 0.55 is observed for $S=1$, which is the original image scale. The function of false detections shows a different trend. The ratio of

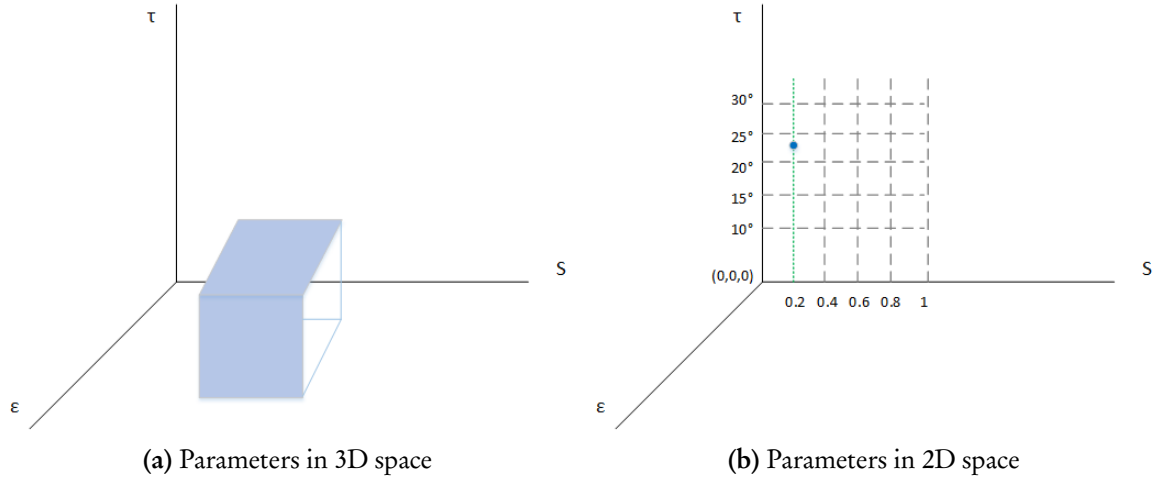


Figure 5.1: The set of the optimal parameter values of the algorithm is a point in the 3D space (a). Each parameter is tuned while the other two are fixed. The tuning process is represented by a line in 2D space (b).

Table 5.1 Distance thresholds $d_r(m)$, $d_e(m)$ and error ratios N_M , N_F for varying scale factor S . Small S values indicate coarse spatial resolution. Higher S values result in finer spatial resolution.

S	$d_r(m)$	$d_e(m)$	N_M	N_F
0.05	643	5029	0.53	0.10
0.1	322	1315	0.51	0.02
0.15	214	524	0.38	0.21
0.2	161	475	0.39	0.22
0.25	129	320	0.40	0.26
0.3	107	279	0.39	0.27
0.4	80	164	0.43	0.39
0.5	64	84	0.49	0.58
0.6	54	79	0.50	0.57
0.7	46	68	0.52	0.59
0.8	40	60	0.51	0.66
0.9	36	57	0.53	0.70
1	32	51	0.55	0.72

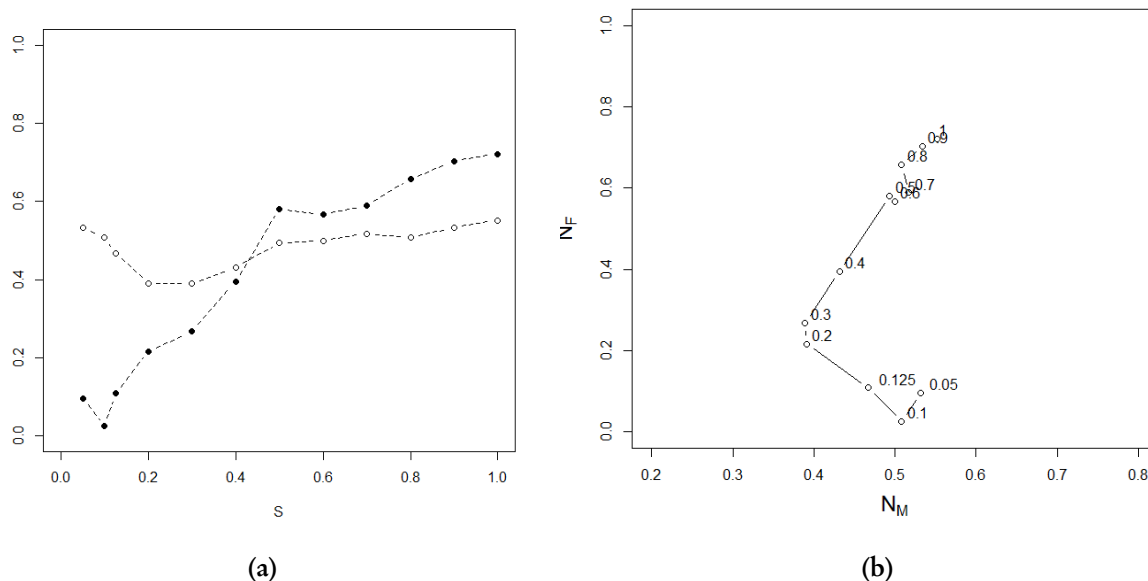


Figure 5.2: Ratio of missing (N_M) and false (N_F) detections for varying scale factor S . (a) N_M (open circles) and N_F (closed circles), lines are added to assist interpretation. (b) N_M against N_F . An optimum is observed in the interval 0.2-0.3

false detections starts from a minimum of 0.02 for $S=0.1$ and steadily increases for $S>0.1$, with an exception at $S=0.05$, where the ratio is larger than the one observed at $S=0.1$. The maximum value (0.72) is again noticed at $S=1$.

Figure 5.2b is a plot of N_M against N_F . In the graph, an optimum is observed at the interval (0.2,0.3). This interval is also a break point of the function. The trends observed for values of S larger than 0.3 and smaller than 0.2 are contrasting. Therefore, the choice is left between the values 0.2 and 0.3. The value $S=0.25$ was also tested. It does not indicate a new optimum, since it lies on the line defined by points 0.2 and 0.3 of Figure 5.2b. The point is excluded from the graph for presentation reasons.

N_M is the same for both values, while N_F is smaller for $S=0.2$. In principal, that points to the value $S=0.2$. Nevertheless, from visual inspection of the result, an important difference is observed between the result for $S=0.2$ and $S=0.3$. For $S=0.2$, as well as for all values $S<0.3$, the result is deteriorated and the nature of the detected segments is lost. The individual segments are merged into one extended object (Figures 5.3a and 5.3b). So, the value for which false detections are minimum and, at the same time, the result is visually correct is 0.3 (Figure 5.3c), which coincides with the minimum of missing detections. The final pixel size for this scale is 50×50 m ($15/0.3 = 50$).

It is concluded that in fine resolutions the result consists of multiple, small segments (Figure 5.3d). In coarse resolutions, the number of detected segments is smaller, as small ones are coerced into larger ones.

5.3 TUNING OF ANGLE TOLERANCE

This section contains the tuning of the angle tolerance. The scale factor is now fixed at a value of 0.3 and ε is kept fixed at 1. Since the scale factor is fixed, the distance threshold d_r is constant.

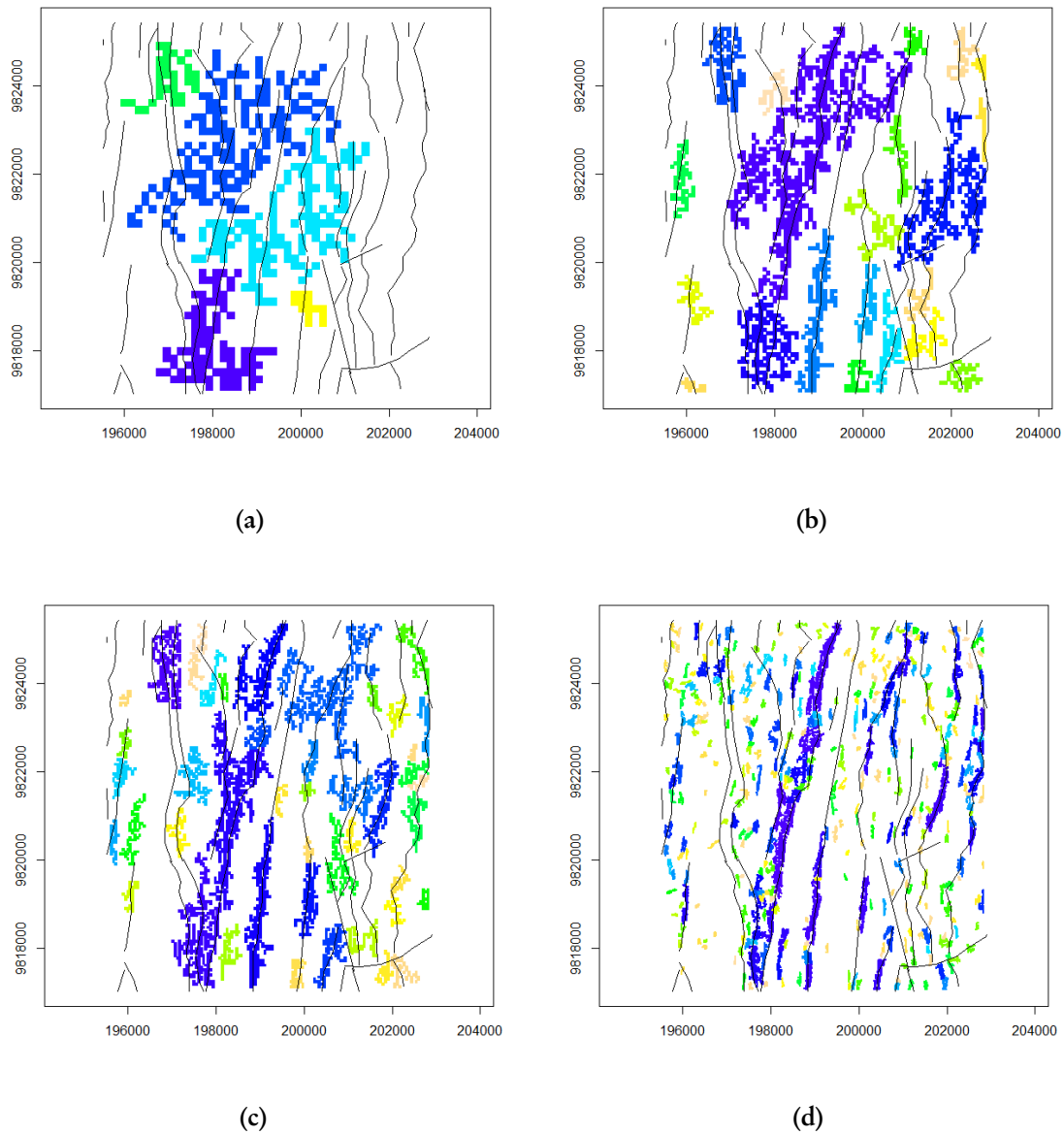


Figure 5.3: Detection results for different values of the scale factor S . (a) $S=0.1$ All the lineaments are merged and detected in five, wide segments. There is no semantic correspondence between reference and extraction. (b) $S=0.2$ The same phenomenon as in (a) is observed, but limited. (c) $S=0.3$ The coarser scale at which the detected segments have correspondence to the reference. (d) $S=0.9$ Many small segments are detected. Many false detections are also observed. Each segment is represented by a different colour. The reference lines are overlaid in black. As we move from coarse to finer scales, the detection consists of more, shorter and smaller segments. In coarse scales, multiple lineaments tend to be grouped in a wide segment.

Table 5.2 Distance threshold d_e and error ratios for varying angle tolerance (τ)

τ°	$d_e(m)$	N_M	N_F
10	146	0.71	0.30
12.5	196	0.62	0.24
15	223	0.54	0.25
17.5	260	0.43	0.21
20	279	0.37	0.24
22.5	298	0.33	0.25
25	300	0.29	0.27
27.5	325	0.26	0.26
30	353	0.21	0.25
32.5	510	0.20	0.14
35	584	0.18	0.13

The tested values of angle tolerance were in the range $[10^\circ, 35^\circ]$ at intervals of 2.5° . The choice of the range was such that the angles grouped together can always be considered aligned, in a strict or less strict frame. Again, the intervals were densified where there was need for more points in order to obtain a clear representation of the error functions. Results are presented in Table 5.2.

The plot of missing and false detections for the several values of τ (Figure 5.4) helps understand the pattern of each type of error in relation to the angle tolerance. To start with, N_M has a decreasing pattern, moving from low to higher values of angle tolerance. That means, the stricter the angle threshold, the larger the N_M . Very few missing detections occur for large angle tolerance values. N_F is within a smaller range, with less variation. The lower values are observed for $\tau > 30^\circ$.

The point at which the two ratios have minimum values and, at the same time, the result proves to be acceptable from visual interpretation is sought. From the graph of Figure 5.4, the minimum point for both ratios is at $\tau = 35^\circ$. N_M might be even lower for larger values of τ , as the trend seems to have a constant descending tenor. N_F , on the other hand, has a more irregular shape.

Visual inspection of the result depicts that for large values of τ the segmentation result is distorted. Lineaments that are close and have similar orientations are detected in fewer, wide segments (Figures 5.5c and 5.5d). That means that the object correspondence between reference and extraction is lost. Hence, the decision cannot be exclusively based on the diagram of Figure 5.4, but it also has to be combined with visual assessment of the result, since the error ratios can be misleading. A characteristic example is that for $\tau = 35^\circ$, where both N_M and N_F are low, but visual inspection depicts a deteriorated result.

The value of τ for which missing and false ratios are as low as possible, while the correspondence between reference and extraction is preserved is 25° (Figure 5.5b). This correspondence is lost for all higher values of angle tolerance. Angle tolerance is fixed at $\tau = 25^\circ$. The maximum difference in angles at which a pixel is still assigned to the *line-support region* is illustrated in Figure 5.6.

In general, small angle tolerance values result in narrower segments. For low τ values, there are many missing detections. The size of the objects and particularly the width increases for large angle tolerance values. For values above 27.5° the result is a single or very few segments that condense all lines in one object. It is clear that at those cases the nature of the segments is lost, since the result are extended polygon segments that have no correspondence to the reference lines.

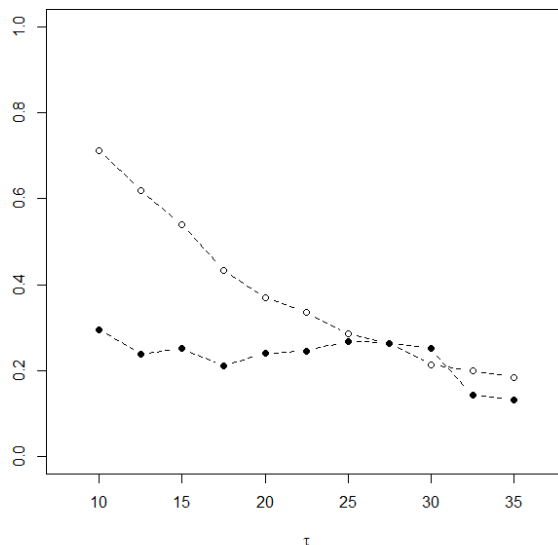


Figure 5.4: Missing (N_M) and false detections' ratio (N_F) for varying angle tolerance (τ°). Open circles: N_M , closed circles: N_F , lines are added to assist interpretation.

5.4 SCALE FACTOR REVISITED

It has been explained in Section 5.1 that parameters are treated individually. For this reason, once the value of angle tolerance is tuned, there is a need to confirm that the choice of the scale factor value (S) that was made earlier is the optimal. So, the ratios of missing and false detections were recorded for $\tau = 25^\circ$. The results are summarized in Table 5.3. Figure 5.7 presents both ratios in a graph.

From the graph it is inferred that the S value for which both N_M and N_F are minimum is 0.2. In Section 5.2 it has been observed that S values lower than 0.3 deteriorate the result and distort the nature of the mapped linear segments. The same phenomenon can be confirmed here visually from Figure 5.8. From this figure the value 0.3 is clearly preferred over 0.2, since the detected segments resemble the form of the reference lines. Hence, the choice of S=0.3 is confirmed.

5.5 TUNING OF THE NFA THRESHOLD PARAMETER ε

The third parameter to be tuned is the NFA threshold ε . Usually this value is set to 1 with no further tests (Desolneux et al., 2001; Desolneux et al., 2003). It is interesting to observe the trends of the errors with the variation of this parameter and decide whether the value 1 is indeed the optimal for this application. The intention is to check the result of allowing segments with high probability of occurrence in a white noise image to pass the NFA check. On the other hand, it is desirable to inspect the result when strict thresholds are imposed and only segments with low probability in the *a contrario* model are accepted. So, some values above 1 were tested, as well as some very small ones, below 1. The results are presented in Table 5.4.

In Figure 5.9 we see the behaviour of the two kinds of errors for the tested ε values. As it was expected, for values below one, the percentage of missing detections goes up and the opposite happens for false detections. High ε values mean less strict threshold, which allows less meaningful segments to pass the NFA control (Figure 5.10). Many of these detections, however, are false.

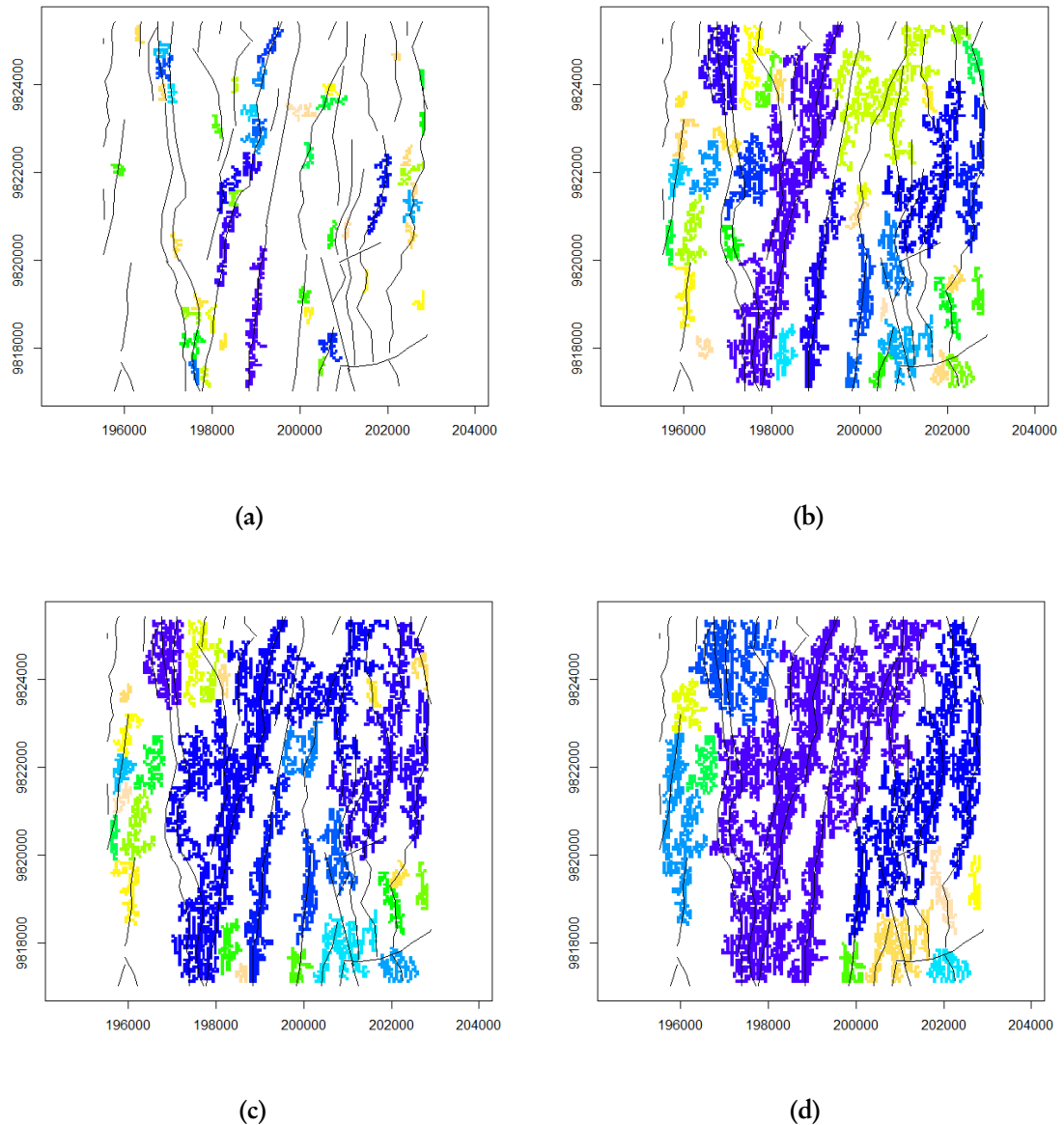


Figure 5.5: Detection results for different values of the angle tolerance (τ). (a) $\tau = 10^\circ$ Many missing detections. (b) $\tau = 25^\circ$ Correspondence between reference and extraction is observed. (c) $\tau = 27.5^\circ$ Close and parallel lineaments start to be merged in big segments. (d) $\tau = 35^\circ$ Very few and large segments are formed. Low values of angle tolerance result in many missing detections. Very large values produce few and big segments, where individual lineaments are coerced in one object.

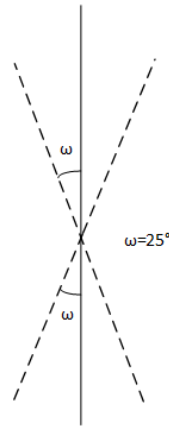


Figure 5.6: The figure shows the maximum accepted angle difference for the region growing. The solid line represents the region angle and the dashed line the *level-line angle* of the pixel to be added in the *line-support region*.

Table 5.3 Distance thresholds and error ratios for varying scale factor S and fixed angle tolerance at $\tau = 25^\circ$

S	$d_r(m)$	$d_e(m)$	N_M	N_F
0.1	322	986	0.37	0.06
0.2	161	446	0.22	0.21
0.3	107	300	0.29	0.27
0.4	80	196	0.36	0.37
0.5	64	98	0.42	0.54
0.6	54	101	0.57	0.51
0.7	46	82	0.46	0.55
0.8	40	66	0.45	0.63
0.9	36	58	0.49	0.69
1	32	55	0.47	0.70

Further, we note that for values in the range $[1, 4]$ the ratios of missing and false detections are almost equal. For values above 4 missing detections are reduced and false ones increase. The opposite pattern is observed for values of ε below 1, where false detections are limited and more missing are recorded. The ratios of missing and false detections are equal for $\varepsilon = 2$.

The number of accepted segments for some ε values is presented in Table 5.5. The lower the value of the threshold, the less segments are accepted. The number of accepted segments for $\varepsilon = 1$ and 2 is 37 and 38 respectively. We note that the difference is only one segment.

In principle, any of the values in the range $[1, 4]$ can be selected. If a value above 1, however, is selected, then segments that could also occur in a random image will be accepted. The value of ε is, therefore, fixed at 1.

5.6 ACCURACY OF THE RESULT

The resulting image after the tuning of all three parameters is found in Figure 5.11b. The ratios of missing and false detections for this parameter values are $N_M = 0.28$ and $N_F = 0.27$ respectively. The two ratios are in balance.

Table 5.4 Distance threshold d_e and error ratios for varying ε for fixed scale factor at $S=0.3$ and angle tolerance at $\tau = 25^\circ$

ε	$d_e(m)$	N_M	N_F
10^{-10}	574	0.56	0.06
0.001	373	0.33	0.19
0.01	332	0.28	0.23
0.1	322	0.28	0.25
0.5	322	0.29	0.25
0.75	300	0.29	0.27
1	300	0.28	0.27
2	307	0.26	0.26
3	299	0.26	0.27
4	291	0.26	0.28
5	291	0.27	0.28
6	294	0.27	0.28
8	288	0.26	0.29
10	288	0.26	0.29
50	261	0.25	0.32
100	235	0.24	0.36

Table 5.5 Number of ε -meaningful segments for some ε values

ε	Number of ε -meaningful segments
10^{-10}	10
1	37
2	38
50	47

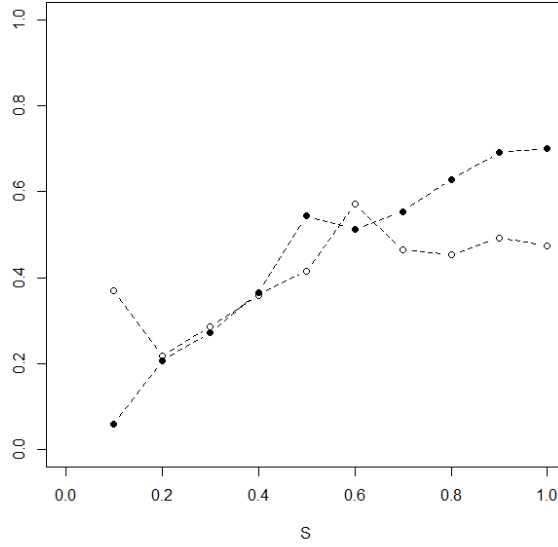


Figure 5.7: Missing (N_M) and false detections' ratio (N_F) for varying scale factor S and $\tau = 25^\circ$. Open circles: N_M , closed circles: N_F , lines are added to assist interpretation.

Table 5.6 Mean and standard deviation of distances

	Mean distance(m)	stdv of distance
from reference	40	23
from detection	121	77

After the parameter tuning, the values of the distance thresholds have also been fixed to $d_r = 107$ m and $d_e = 300$ m. The calculation of those thresholds is explained in Section 4.2.4. In Figure 5.12 the histogram of the distances of points between extraction and reference are shown. A line indicates the two threshold values. Points on the left of the threshold line are considered successful detections. The differences in local orientations are treated respectively. Finally, successful detections are those points that fall below both the distance and the angle thresholds and for those the mean distance and its standard deviation are computed (Table 5.6).

The mean distance from the sample reference points to the detected points is smaller than the one measured in the opposite direction. The same holds for the respective standard deviations. Same conclusions are drawn from the histogram, since the frequencies of long distances are much higher when measuring from extracted points (Figure 5.12(b)). This difference is explained by the nature of the objects, which was referred to in section 4.2.4. When starting from reference, the mean distance from the detected points is less than a pixel (50m). Starting from detection, the mean distance does not exceed three pixels.

5.7 ERROR VISUALIZATION

In this section, a visualization of the two kinds of errors, missing and false detections, is presented. Successful and unsuccessful detections are illustrated in two maps (Figures 5.13 and 5.14). The first map (Figure 5.13) is a visualization of successful and missing in detections with regard to the

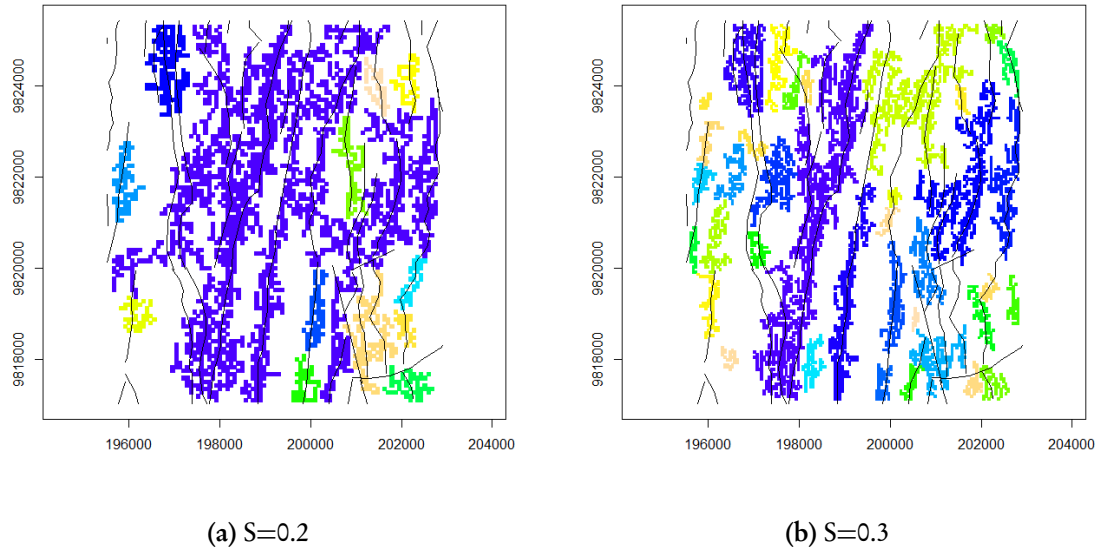


Figure 5.8: Comparison of the detection results for $S=0.2, 0.3$ and $\tau = 25^\circ$

reference lines. As it has been explained in section 4.2.1, interval points have been selected on the lines for the purpose of accuracy assessment. On the map, we see in green interval points for which a corresponding point has been found in the set of detected points. Correspondence premises at least one point in close distance, with similar local orientation. It implies that the particular interval point has indeed been detected. In red are the points for which no correspondence was found. This map is a presentation of the completeness of the final detection result.

The second map (Figure 5.14) is a plot of true and false detections and concerns the detected points. In green are the detected points for which a corresponding point has been found with the reference. Correspondence is mentioned in the same context as before. Green points indicate true detections. Red points have not matched with any interval point of the reference and are, consequently, false detections. This map is a visualization of the correctness of the result.

Next, the most prominent error cases are pointed out by some plots on the image (Figure 5.15). To start with, several cases where missing detections have been identified. The most prominent concerns a lineament that is not represented by a line, at the particular region of the image (plots A and F, Figures 5.13 and 5.15). Another frequent case, which is a sub-category of the previous case, concerns lineaments that do not correspond to an edge and have been delineated by the interpreter based on experience (plots C and E). Geological experience allowed to connect individual lines that are likely to belong to the same structure (Woldai, October 2013). Missing detections are also observed where lines have strong curvature, and the line detector fails (plot B). Finally, weak edges are also sometimes not detected (plot D).

The causes of false detections are fewer. The most clear case is that of edges that do not represent lineaments (plots 1 and 2, Figure 5.14). It is expected that on the image several edges are visible. Not all of them point to a geological feature or are considered to be such from the interpreter. Secondly, false detections occur where the whole fault plane or even the sediment that has covered the part between two lineaments is detected (plots 3 and 4).

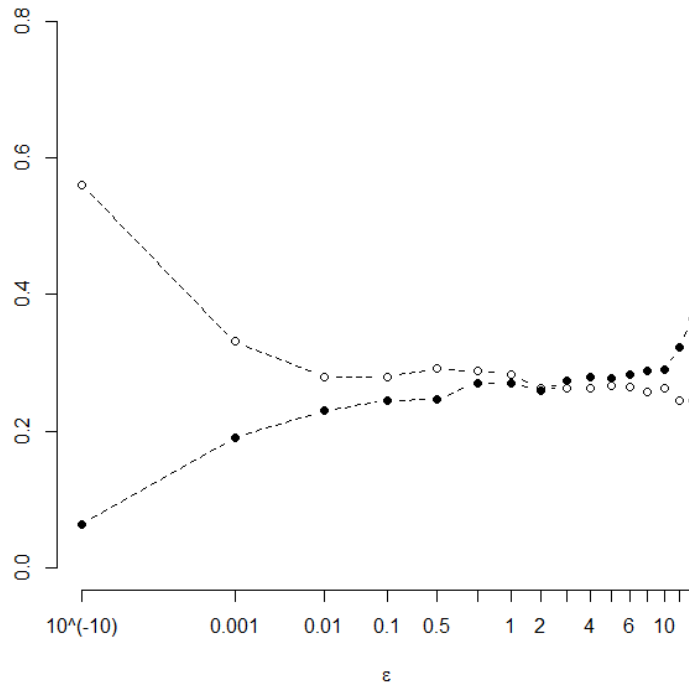


Figure 5.9: Missing (N_M) and false detections' ratio (N_F) for varying ϵ (plotted in log scale). Open circles: N_M , closed circles: N_F , lines are added to assist interpretation.

5.8 DETAILED ASSESSMENT OF THE DETECTED SEGMENTS

In the previous sections it has been deduced that the present method cannot provide a standalone measure of the quality of the result and it always has to be assisted by visual interpretation of the result. The main problem that is tackled here is the comparison of two sets of objects with different geometrical properties. Lines from the reference dataset and groups of points from the detection. For this reason, in this section the relationship between the two sets of objects is explored, by focusing on one example. A pair of a reference line and its corresponding segment was selected for this purpose (Figure 5.16). The selected lineament is a clear edge that represents a major structure. In addition, it is being detected by a single segment, which means that there is an one-to-one correspondence between reference and detection. For these reasons, the particular pair was selected as a starting case for a simple example towards the description of the correspondence between the two objects. If further analysis is to be performed, then more complicated relationships should be explored, such as the cases where one reference line is detected by multiple segments or where a segment is representing more than one reference lineaments.

The applied approach and measures are described in Section 4.3. The example here refers to certain parameter values that have proven to be critical from the analysis in the previous sections.

First, the result for some scale factor (S) values is explored. The results are presented in Table 5.7. Segment points are usually distributed on both sides of the line. The distribution of the distances, however, is never equal. There are cases that the difference is not great ($S=0.2, 0.6$) and others where one side is obviously favoured over the other ($S=0.3, 0.4, 0.9$). In general, the ratio of hits in the Table 5.7 indicates successful detections. That was expected, since the line and segment were

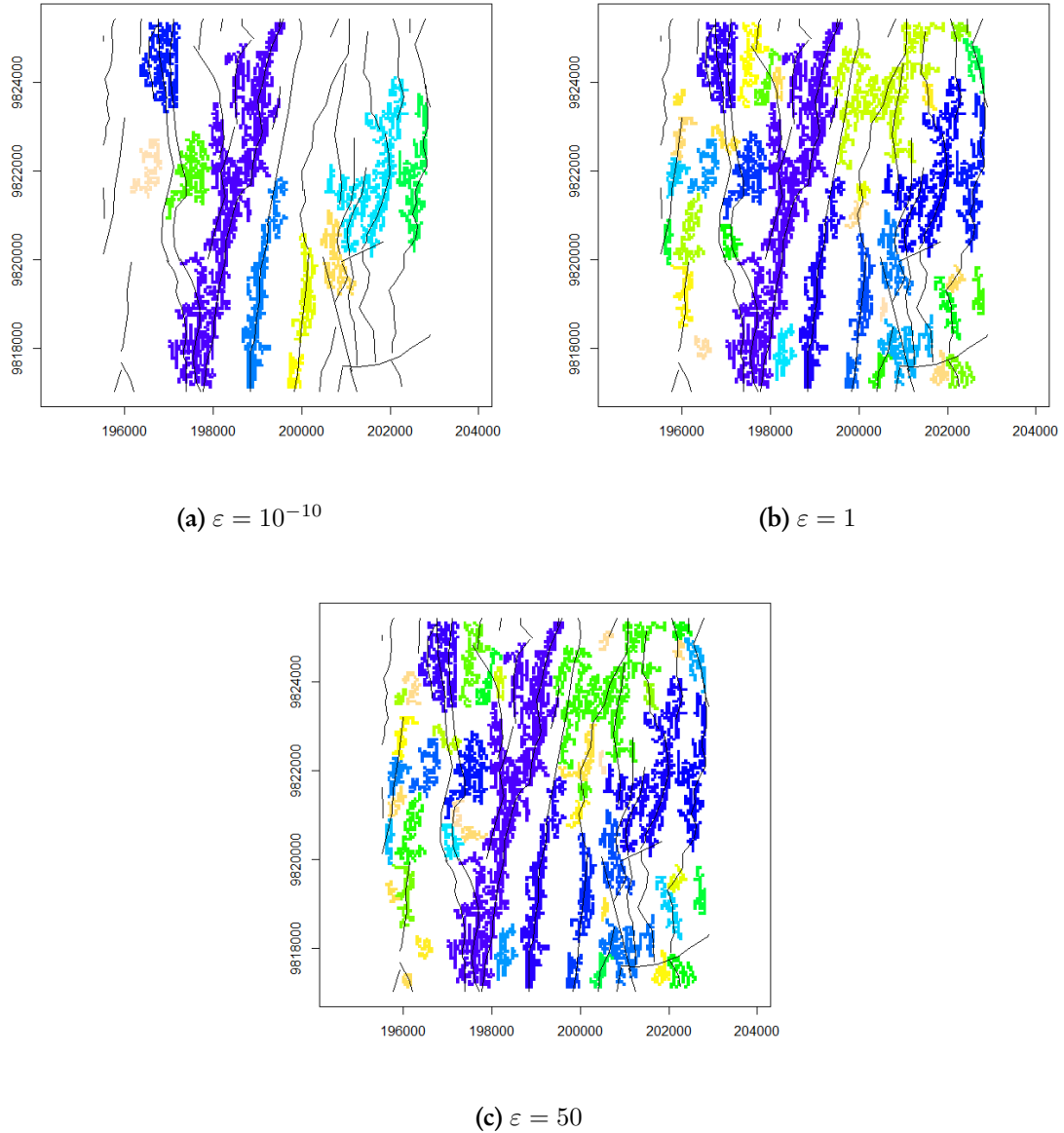


Figure 5.10: Detection results for different values of the NFA threshold (ε). Very low thresholds result in the acceptance of less segments. For high values, more segments are accepted, since segments with higher NFA pass the control, and false detections occur.

Table 5.7 Distribution of the distances between reference and detected points and ratio of hits for some scale factor values. All distances reported in meters.

S	Mean distance		Ratio		Standard deviation		no points	hits
	Left	Right	Left	Right	Left	Right		
0.2	147	173	0.46	0.54	67	122	45	1
0.3	110	81	0.58	0.42	70	55	67	0.91
0.4	102	66	0.61	0.39	53	40	92	0.99
0.6	65	53	0.55	0.45	33	23	137	0.99
0.9	53	38	0.59	0.41	35	25	206	0.88

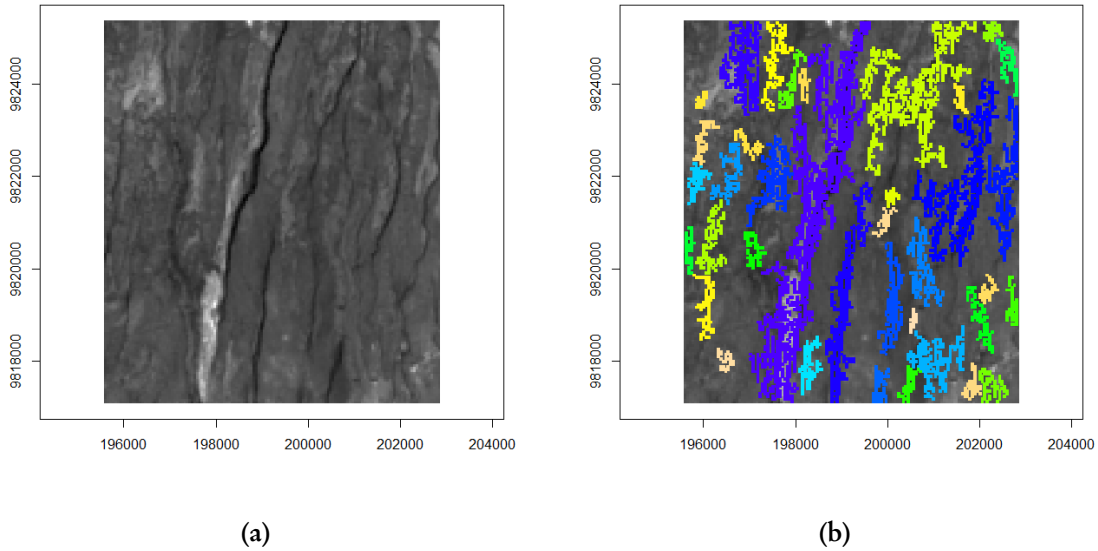


Figure 5.11: (a) Sub-sampled image with $S=0.3$ and (b) Final detection result

chosen for showing clear correspondence. The lowest ratio of hits occurs for $S=0.9$. The order of magnitude of the mean distance is the same for all scale factor values. Some results are illustrated in Figure 5.16.

The most important observation is that, in almost all cases, the ratio of distances on the left is higher than the one on the right. This relationship between the two objects can be explained on the basis of the manual interpretation explained in Section 3.3. The present example is a typical case of interpreting the actual position of the lineament, where both the lineament and scarp are visible on the image. The dark part of Figure 5.16a represents the fault scarp, which is narrow and has two bounding edges (Figure 3.5b). One of them is the actual lineament and this is where the reference was delineated. In image analysis terms, on the other hand, both edges are detected and since they are parallel and close together they are detected by a single segment. This is the reason why the particular relation between the two objects is observed.

Next, the scale factor parameter is fixed at $S=0.3$ and some angle tolerance values are tested. The results are presented in Table 5.8. The same pattern is observed here; the ratio of distances on the left is constantly higher than the ratio of distances on the right. Some differences in the magnitude of the mean distance is observed. For the values $\tau \in [22.5^\circ, 27.5^\circ]$ the mean distances are almost equal. For extreme low or high values those change. It has been stated before that for such extreme values the result is being distorted. Two examples are shown in Figure 5.17.

From all the above it is deduced that geological experience is essential in order to translate an automatically detected segment into a line that corresponds to a lineament. In particular, this knowledge will define the respective position of the segment at which the lineament is located. On the other hand, the geometry of the detected segment can testify about the characteristics of the lineament. Specifically, the width of the detected segment is related to the steepness of the plane of the crusting. The steeper the plane, the narrower the segment that is apparent on the image.

There are a few points that can be discussed on the comparison of these results to the previous accuracy measures. First, this assessment method, in contrast to the validation method, exploits

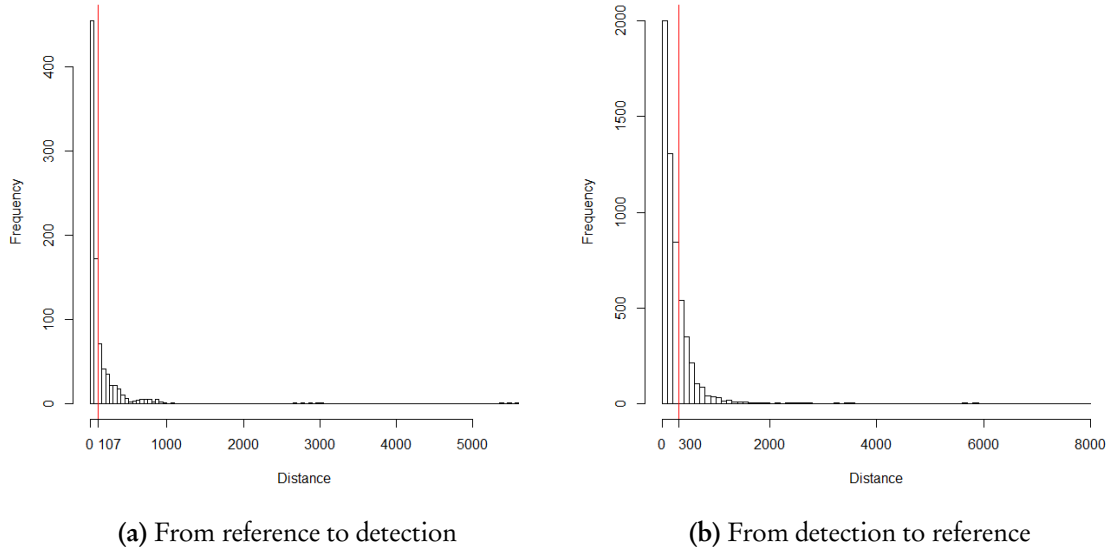


Figure 5.12: Histogram of distances measured from reference to detected points and vice versa. A threshold is applied to distinguish successful and unsuccessful detections. The threshold is illustrated with a red line corresponds to d_r and d_e for (a) and (b) respectively. Points on the left of the threshold lines are considered successful detections.

Table 5.8 Distribution of the distances between reference and detected points and ratio of hits for some angle tolerance values. All distances reported in meters.

$\tau(^{\circ})$	Mean distance		Ratio		Standard deviation		no points	hits
	Left	Right	Left	Right	Left	Right		
12.5	57	57	0.50	0.50	57	47	68	0.88
22.5	107	80	0.57	0.43	69	54	67	0.91
25	110	81	0.58	0.42	70	55	67	0.91
27.5	111	89	0.56	0.44	70	60	67	0.91
35	229	110	0.68	0.32	255	67	68	0.99

only distance and not orientation measures. On the distance measures, if the mean distances resulting here are compared to the distance thresholds applied previously (d_r , Table 5.1) it is derived that there are very few points on the left of the lineament that would have been rejected by the validation method. These are the points at the greater distances. Note that the distance threshold d_r for scale factor $S=0.3$ was 107m and the mean distance of the points on the left is 110m. Both mean distances on the left and on the right (110 and 81m respectively) are close or below the threshold d_r , which confirms that this threshold accepts clearly corresponding detections, like the one presented in this example.

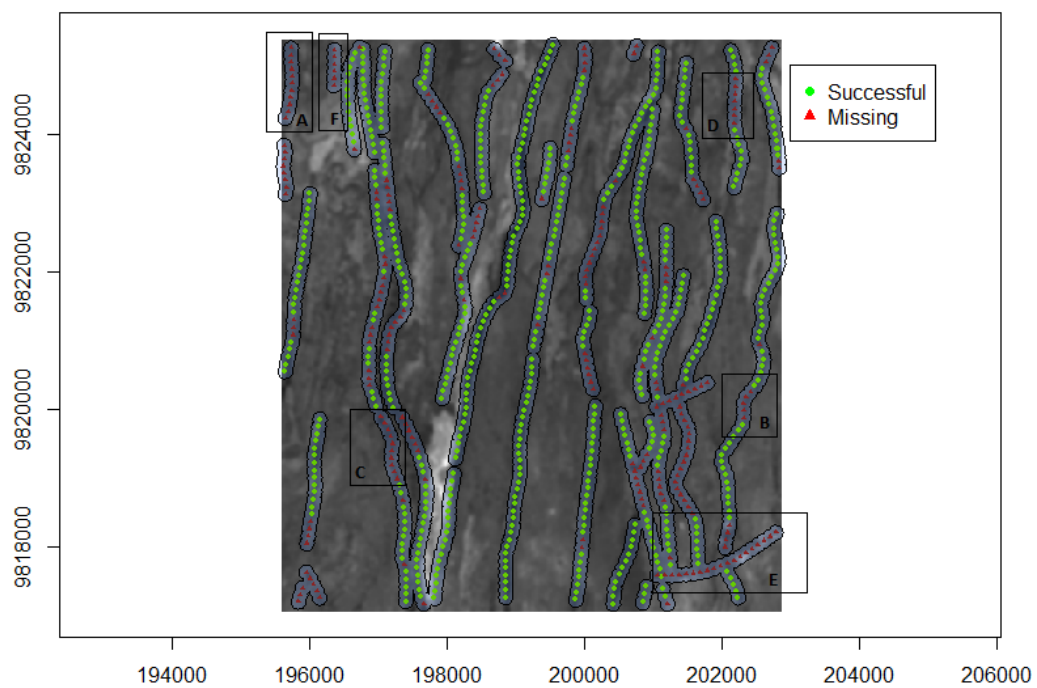


Figure 5.13: Successful and Missing detections. The measure concerns the interval points drawn on the reference lines. In green, reference points that have been detected. In red, reference points that have not been captured by the detection. The distance threshold d_r is illustrated with the blue buffer around the reference points.

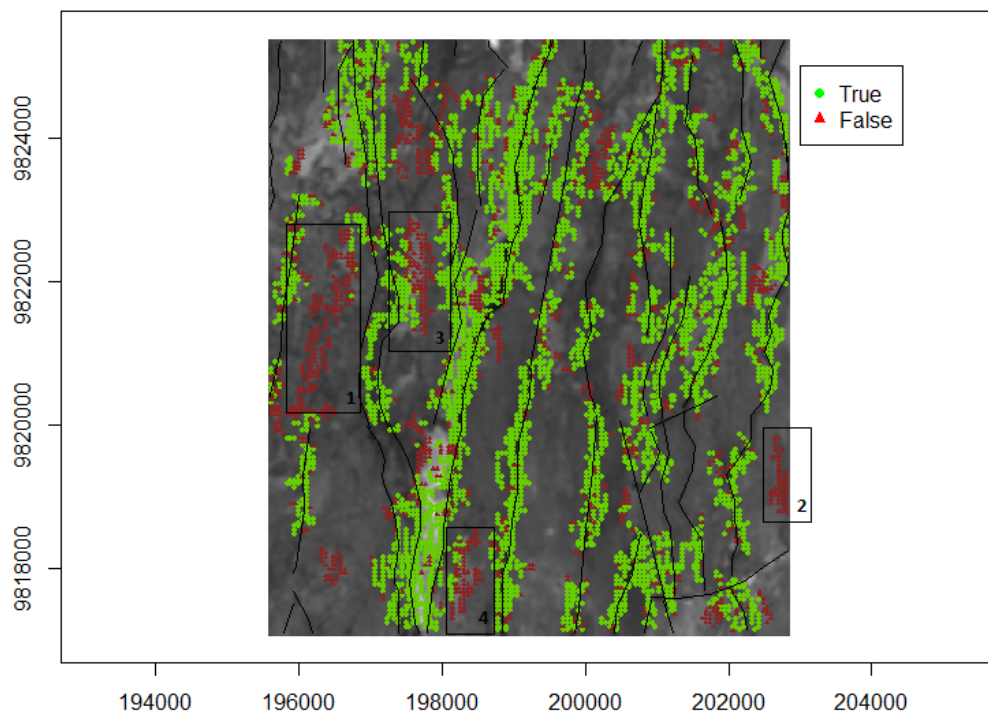


Figure 5.14: True and False detections. In green are detected points that correspond to the reference. In red, false detections.

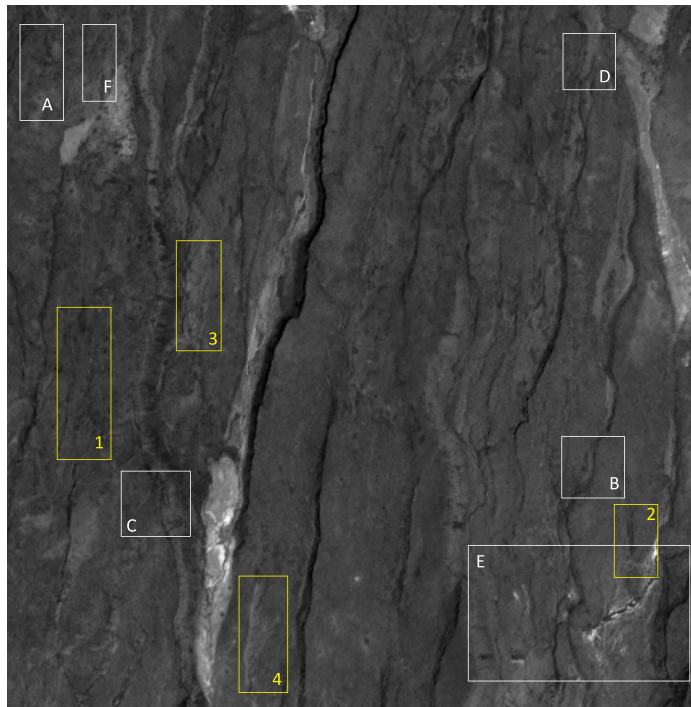


Figure 5.15: PC1 of the ASTER image. Regions of missing detections are indicated with the letters A-F. Regions of false detections are indicated with the numbers 1-4.

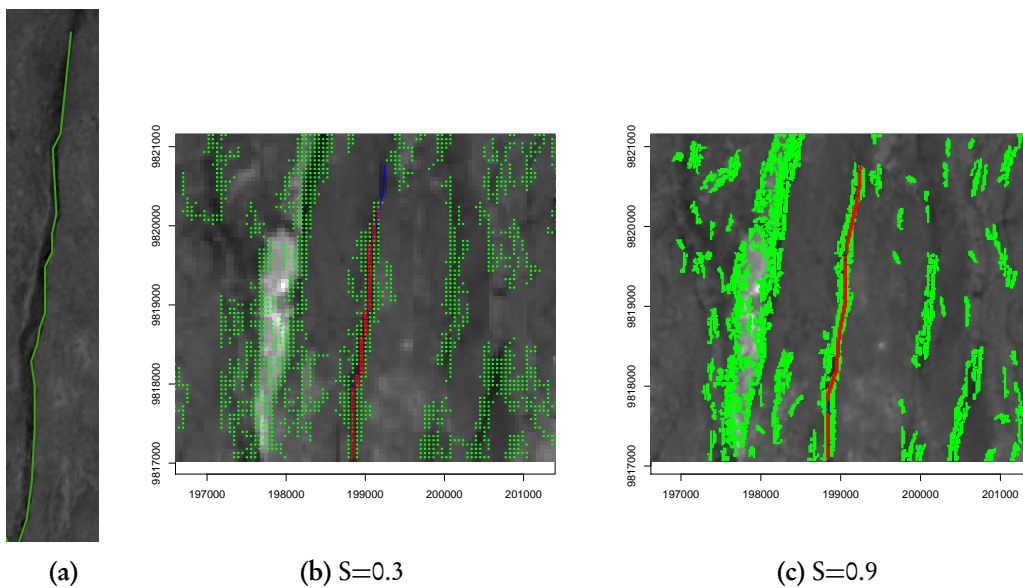
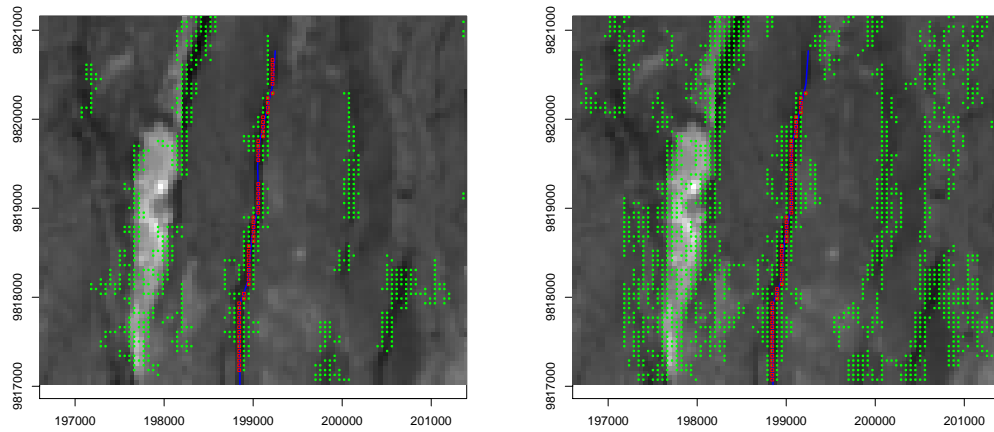


Figure 5.16: (a): Lineament and the interpretation. The fault plane is also visible in the image in dark colors. (b),(c): Detection result and reference line. The reference line is drawn on the right, in the transition from light to dark (right to left), where the crusting is happening. Hits are corresponding points between reference(blue) and detection(green) and are indicated in red.



(a) $\tau = 12.5^\circ$

(b) $\tau = 27.5^\circ$

Figure 5.17: The distribution of extracted points around the reference lines, for two different angle tolerance values.

Chapter 6

Discussion

6.1 LINEAMENTS ON REMOTELY SENSED IMAGES

All geological lineament definitions encountered in literature speak of linear features (Hobbs, 1904; O'Leary et al., 1976; Clark and Wilson, 1994; Hung et al., 2005). When it comes to lineament interpretation from satellite images, however, this definition is not directly applicable. Depending upon the spatial resolution, the topography, the satellite viewing angle, the sun angle, as well as the type of lineament, the outline of the lineament might differ from a discrete line and be part of a planar feature. This is mainly encountered for normal faults, which are the prevalent structures of the area around Lake Magadi (Atmaoui and Hollnack, 2003). If the slope of the faulting is shallow and the viewing angle is almost perpendicular to the plane of the fault, then the latter is projected and clearly visible on the image. In the opposite case, where the fault scarp is not visible (e.g. on the other side of the graben), the slope may create a wide shadow that extends further from the fault trace. In both cases, in the image a polygon appears that stands out from the background landscape and it is hard to distinguish the fault scarp from the fault trace, which is in fact where the crusting happens. This issue concerns both automatic lineament extraction and manual interpretation. It is expert knowledge that helps overcome those ambiguities and delineate the geological feature on its accurate position. This problem cannot be completely solved by experts either, and interpretation is still dependent on those conditions.

This problem is related as well to the spatial resolution of the image and the scale of the representation. The coarser the resolution, the representation of the lineaments is closer to a line. Yet, the extent of those planar features varies. A downscaling factor should be defined for the image, such that no wide polygon features are observable and still all lineaments are detectable. Downscaling of the image to the resolution that would result in the most complete and correct detection was one of the main points this research tackled. The selection of the optimal scale was carried out with the tuning of the scale factor S . The resulting spatial resolution was 50 m, over the original of 15 m.

The result of the segmentation algorithm in our case is line support regions, which potentially represent geological lineaments. The effect of the factors described here is that those regions are in most cases polygon features, rather than lines, since the scarp or its shadow are also detected as components of the segment.

The relationship between reference lines and detected segments was explored for a selected segment. It is inferred that geological knowledge can be exploited in these cases in order to relate the detected polygon features with the actual position of the lineament. The set of criteria for geological interpretation can be used in order to transform the image result into linear features and place them in the respective location of the lineaments. The detection result, on the other hand, can provide useful information about the characteristics of the geological structures. The width of the segments is directly related to the steepness of the slope of the fault scarp. A shallow slope is projected as a wide polygon feature on the image and produces wider segments. Steep slopes have a narrow shape and the detection result is closer to a line, rather than a polygon.

The Line Segment Detector (LSD) algorithm, that was used as a starting point for this study has been tested in close range images that contain mainly man-made objects. In close range imagery, the boundaries of solid objects are usually straight, clear and narrow lines. This is not the case for natural objects on images of moderate spatial resolution. The boundaries and the lines are rather fuzzy. The evaluation of the detected segments against the *a-contrario* model uses an associated geometrical shape that describes the geometry of the first. Here, a rectangle was used to represent each segment and the NFA was calculated on this basis. It is understood, however, that the more the segments deviate from straight lines, the less a rectangle describes its shape. Depending on the shape and form of the objects to be detected, either those are geological lineaments or not, the shape used for the evaluation step of NFA can be chosen accordingly in future research.

Another characteristic of Remotely Sensed images is the presence of noise. This relates also to the definition of the orientation, which is encoded by the *level-line angle*. According to Grompone von Gioi et al. (2012), the *level-line* angle points the direction of the edge that crosses the pixel in question. This assumption can be proven to hold for clear lines in close range imagery. Geological edges, as in this study, however are much more noisy, resulting in noise in the *level-line angles*. Their use for the rectangle approximation was satisfactory, judging the result visually. Their use for local orientation calculation of the segment points was more challenging. The effect of the noise on them was stronger. For this reason, it is suggested that the use of the *level-line angles* in the validation method, as a means of extracting the local direction of the segment points is revisited and that alternative direction measures are explored.

In this study, the three bands in the visible and Near Infra-red (VNIR) range of the ASTER image were used, since these are those most commonly used in literature for lineament interpretation (Woldai, October 2013). The contribution of bands in the Short Wave and Thermal Infra-red (SWIR and TIR) spectrum can be explored in the future. Multispectral information was exploited by performing Principal Components Analysis (PCA) of these three bands. Sum of gradients of all available bands is an alternative option for multi-spectral data handling, but was not explored in this research due to time constraints.

6.2 UNCERTAINTY IN LINEAMENT INTERPRETATION AND AUTOMATIC DETECTION

Expert knowledge and experience are essential in geological lineament mapping tasks. Subjectivity commonly plays a role and different experts may produce controversial results (Gómez and Kavzoglu, 2005). Subjectivity in the lineament identification is related to the extent as well as the existence of the lineaments (Ramli et al., 2010). Differences can also be noted if the same observer is asked to interpret the same image in different points in time (Mabee et al., 1994). Thus, it is suggested that the more object coincidences we get from different observers, the more confident we can be that the extracted lineaments correspond to a geological structure in reality (Mabee et al., 1994).

There is clearly no definite and unambiguous interpretation of geological lineaments. Instead, there can be several different interpretations of the same area, from different geologists. Therefore the results obtained in this study are inside the limitations that a single reference dataset (interpretation) implies. Parameter tuning was based on parts of a single interpreted lineament map. One can expect to get slightly different results if a separate interpretation is used.

Particularly for the formation of objects, geologists use their experience to connect individual segments on the image and form longer lineament units (Wang and Howarth, 1990). The set of criteria used for delineation and connection differs between experts (Wladis, 1999). Therefore, the

definition of a *lineament unit* is not solid and definitive. The starting and end point of a lineament as well as its connectivity to others, in terms of geological significance is not certain.

Another important factor related to the definition of a lineament *unit* and its connectivity to others is the scale of the image. Short lineaments that have similar directions and occur in sequence with breaks in between will eventually appear as a single long lineament if the image is rescaled to a lower spatial resolution. It is again hard to decide on the extent of a complete lineament *unit*. Besides, the delineation of the reference dataset used in this study was carried out in a particular image scale which is not necessarily the optimal for automatic mapping.

We conclude that the effort to link our result to the reference, by establishing an *one-to-one relationship* of the features would run the risk of over-fitting the procedure to the particular dataset, without assuring that the formed objects are best representing the geological setting in question. For this reason, the method developed for validation did not incorporate any step of feature matching between reference and extraction. Such an approach would force the result to fit as much as possible to the given reference data, without any gain in the detection method.

At this point it should be noted that the current method aims at detecting all edges on the image. As a result, even edges that do not represent geological lineaments can be detected and give false detections for the purpose of this application. In our study area, this is not a major problem once the drainage network is not dense and no transport (roads, railway) network is present. In areas where such linear features exist the algorithm will not make a distinction between those. A way to deal with this interference is to extract all other linear networks from the image before the detection.

6.3 VALIDATION METHOD

One of the main parts of this research has been to develop a validation method that would provide quality measures of the result and would allow to quantitatively estimate the optimal parameter values for the specific application. Several validation methods exist in literature for the comparison of automatically extracted lines and a reference. The challenge of this research, however, has been that the comparison had to be implemented between two objects of different geometrical type. As a result, none of the standard methods could be used. The idea of the validation methodology was based on a positional accuracy measure by Goodchild and Jeansoulin (1998). The approach was further extended and instead of using only distance measures, a measure of the difference of the orientations of the compared objects was added. The result is assessing not only the positional, but also the directional accuracy of the result. Furthermore, since the lineaments were not perfectly straight lines, the global measures were replaced by local ones, such that the orientation of the objects was sufficiently described at every point.

Two error ratios were defined, the ratio of missing and false detections. These ratios were used for the estimation of the optimal parameter values in parameter tuning. The sequence at which the three parameters were tuned is scale factor S , angle tolerance τ and NFA threshold ε respectively. The reasons behind the order selection are described in section 5.1. Moreover, since the parameters were estimated individually, the scale factor was revisited after the tuning of angle tolerance in order to confirm that the previous choice of S was indeed the one that minimizes both error ratios.

If the selected parameter values are compared to those suggested by Grompone von Gioi et al. (2012) some similarities, as well as some differences are observed. The scale factor that produced minimum errors in this study is $S = 0.3$, while the one suggested by the LSD authors is $S = 0.8$.

It is understood that in this study image sub-sampling is not only applied to eliminate quantization and aliasing problems, but it also relates to the geometrical representation of the geological lineaments on the image and the spatial resolution at which the lineaments are most successfully detected. The difference between the τ value suggested in the LSD implementation and the one resulting from parameter tuning here is small, 22.5° and 25° respectively. Finally, the ε value was fixed here at 1, same as in LSD. It was observed, though, that the error ratios were stable for $\varepsilon \in [1, 4]$.

The question that arises is to which extent the error ratios give insight on the geometrical relationship between the detected objects and the reference lines. It is clear so far that the detected segments are closer to polygon objects rather to lines. The ratios do not give full information on the structure of the objects, with regard to the reference. It was observed in many images that parallel lineaments that have a high density are sometimes detected in a single and wide segment. In those cases, the ratio of missing detections would be low and only the false detections' ratio could inform about the expansion of the segment in big distances from the reference line, stemming from a large sum of the distances. This phenomenon was reduced but not fully eliminated after the parameter tuning.

If the study is to be further extended, there can be an effort to transform the segments into linear features, such that they correspond to standard lineament maps. This could be possibly achieved with the incorporation of knowledge on the geological interpretation that would indicate suitable morphological operations for the skeletonization of the result and its transformation to lines.

For the distinction between successful and unsuccessful detections some thresholds were introduced in the process. The choice of the threshold values was based on the nature and the geometry of the detected segments. Those values can be modified, depending on the required positional and directional accuracy of the extracted segments. The absolute ratios of false and missing detections are indications of the quality of the result, but not strict measures. They have been mainly used as relative measures, in order to pick the optimal parameter values of the algorithm for the particular task.

The error ratios derived from the validation method have described the pattern and have allowed the quantitative comparison of the result for different parameter values. Some challenges were encountered for extreme parameter values, where some error ratios were misleading. Therefore, the method, as it is formed so far, cannot be used as an automatic procedure for validation. It should also be accompanied by visual inspection of the result. Hence, the methodology can be characterised as semi-automatic, assisted by visual interpretation.

The method was built in such a way that it would allow the comparison of the results obtained for different values of the algorithm parameters. Overall, this study explored, on one hand, the nature of the mapped phenomenon and its appearance on satellite images and, on the other hand, their relation to the algorithm elements, such as the scale and the NFA threshold. Consequently, the goal of using an algorithm based on Gestalt theory and the Helmholtz principle for a real GIS application has been accomplished.

The validation method that was developed provides statistical measures that allow parameter tuning and describe the completeness, correctness and positional accuracy of the result. It is a stand-alone method that can be applied for the comparison between automatically extracted lines or polygons and a reference set of lines.

At this point, the dependence of the result on the study area should also be highlighted. The parameter tuning was carried out on a particular scene. The algorithm was not further tested elsewhere. Therefore, the chosen parameter values, as well as the measures of accuracy are inferred from the characteristics of the geological features of the particular area. It cannot be ascertained that the algorithm will produce results of equal accuracy in areas where lineaments have different

geometrical characteristics. It was ascertained, however, that the selected subset contains most of the characteristic geological structures encountered in the area.

6.4 COMPUTATIONAL EFFICIENCY

The algorithm is fully implemented in R. An approximate time for complete run, with the final parameter settings and an image size of 460x520 pixels, is 2 minutes. This time increases significantly for finer spatial resolutions and larger image size. The most computationally demanding steps are the region growing algorithm and the distance calculations for validation.

Chapter 7

Conclusions & Recommendations

7.1 PARAMETER TUNING

After the completion of the tuning process, the algorithm parameters were fixed at certain values based on the results of the validation method and visual interpretation. The measures of the developed methodology provided a description of the trend of the errors for varying parameter values. The quantification of these trends served for the parameter value choice, on the basis of minimizing the errors and keeping, as much as possible, a balance between false and missing detections. It was shown, however, that the tuning method cannot itself provide a fully automatic estimation. There is still a need for visual interpretation of the result, in order to confirm that the value indicated by the method corresponds to an acceptable result. There have been cases, for extreme parameter values, where the error ratios have been misleading.

The choice of the scale factor parameter (S) proved to be critical, since the effect of the scale on the result is strong. This parameter is related to the ratio of false detections. Many false detections occur for scale factors $S > 0.5$. This parameter also controls the number of detected segments. In coarse resolutions this number is small and it increases at fine scales. Finally, its effect is evident on the size of the detected segments. The latter is inversely proportional to the scale factor.

The angle tolerance τ dominates the ratio of missing detections. This ratio is decreasing for higher τ values. It was shown, though, that from a certain τ value and on, although the missing detections' ratio is low, the result is distorted. Further, angle tolerance proved to be strongly related to the shape of the detected segments. Small and narrow segments emerge from low τ values, while wide ones arise from high angle tolerances.

The role of the ε parameter that defines the Number of False Alarms (NFA) control was explored, although in most studies it is set to 1 with no further tests. This parameter defines the number of segments that will be accepted as *meaningful*. The resulting patterns of the errors were as expected. Values of ε below 1 yield very few false and many more missing detections. Values much larger than 1 generate the opposite pattern. In addition, it was observed that for a particular range of ε values ($[1,4]$) the error ratios, as well as, the number of accepted segments was stable.

Further, the relationship between the detected and the reference features was explored, towards the establishment of a coherence between “what a geologist sees as a lineament” and what “the algorithm sees as a meaningful line segment”. This relationship was explored on the basis of an example. From that, it occurred that there is an anisotropy in the distribution of the extracted points along the reference line. More examples should be examined, to get a better insight on the correspondence between features.

7.2 ASSESSMENT OF THE DETECTION RESULTS

According to the adopted methodology, the ratios of missing and false detections derived are 0.28 and 0.27 respectively. It should be stated that these ratios refer to the image subset on which the tuning was performed.

The cases where missing and false detections occur were explored. Missing detections, in most cases, are noticed where parts of lineaments do not appear as edges on the image. Several times, long lineaments are broken into smaller sub-parts, since the part in between is covered by sediment, which is not an edge on the image. The experience of the interpreter allows him to decide whether these sub-parts belong to the same lineament and connect them with a continuous line. This problem cannot be eliminated with the present algorithm, since it is out of the frame of edge detection. Weak lineament edges also often fail to be detected. Finally, lineaments with strong curvature are troubling the detection algorithm, since the latter is a detector of straight segments. A possible way of treating with the particular problem is with a modified region growing algorithm that does not strictly seek straight lines.

False detections mainly occur on edges of the image that do not correspond to any geological feature. In our case, the identity of these lines has not been defined. In general, it would be wise, before proceeding, to extract from the image all the irrelevant linear networks, such as drainage and roads, in order to avoid confusion in the detection. Last, cases where the whole plane of the crusting, that includes both its edges, is detected, more false detections occur. This issue directly connects to the relationship of between the detected object and the actual position of the lineament, as it is found in the reference data (Section 5.8). From one example that was examined in this study, anisotropy was observed in the distribution of the segment points in the two sides of the reference lineament. That means that the reference line does not fall in the middle of the segment but lies closer on one of its edges. This relationship should be further explored and be related to the appearance of the feature on the image (Section 6.1). The conclusions of this exploration can be incorporated in the algorithm and exploited for the establishment of a better correspondence between the automatically extracted segments and the actual position of the lineament.

7.3 RECOMMENDATIONS

For the best understanding and interpretation of the detection result, further exploration of the geometrical correspondence between the detected segments and the reference lines is needed. The conclusions of this exploration along with the incorporation of more elements of geological knowledge on the interpretation could establish a strong connection between automatic detection and manual digitization. The incorporation of this knowledge can serve as a guideline if the result needs to be transformed into linear features. One possible approach would be the application of morphological operations.

The result of the algorithm and the parameter tuning process would be enhanced if more images of neighbouring areas, that contain similar features, were to be used. In addition, it is important to explore the results produced given a different or even several more geological interpretations of the same areas. This way, it is guaranteed that the algorithm is not over-fitted to a particular dataset.

Finally, it is important to compare the results of this algorithm to other standard edge detection methods that are used for automatic lineament mapping purposes.

The present algorithm is not restricted to geological lineament detection. Its scope is linear segment detection on Remotely Sensed images. Examples of such linear features are rivers and roads and the algorithm can be applied for their detection, if adequately adjusted. Parameter settings can be modified and new optimal values can be sought for each particular application using the current validation method. Further, the region growing algorithm is now formed to detect straight linear features. It can be modified according to the specific shape of the objects to be detected and provide an updated algorithm for more detection applications.

Bibliography

- Achauer, U., Masson, F., 2002. Seismic tomography of continental rifts revisited: from relative to absolute heterogeneities. *Tectonophysics* 358, 17–37.
- Atmaoui, N., Hollnack, D., 2003. Neotectonics and extension direction of the southern Kenya Rift, Lake Magadi area. *Tectonophysics* 364, 71–83.
- Burns, J., Hanson, A. R., Riseman, E. M., 1986. Extracting straight lines. *IEEE Transactions on Pattern Analysis and Machine Intelligence PAMI-8* (4), 425–455.
- Clark, C., Wilson, C., 1994. Spatial analysis of lineaments. *Computers and Geosciences* 20 (7-8), 1237–1258.
- Desolneux, A., Moisan, L., Morel, J.-M., 2003a. A grouping principle and four applications. *IEEE Transactions on Pattern Analysis and Machine Intelligence* 25 (4), 508–513.
- Desolneux, A., Moisan, L., Morel, J.-M., 2000. Meaningful alignments. *International Journal of Computer Vision* 40 (1), 7–23.
- Desolneux, A., Moisan, L., Morel, J.-M., 2001. Edge detection by Helmholtz principle. *Journal of Mathematical Imaging and Vision* 14 (3), 271–284.
- Desolneux, A., Moisan, L., Morel, J.-M., 2003b. Maximal meaningful events and applications to image analysis. *Annals of Statistics* 31 (6), 1822–1851.
- Desolneux, A., Moisan, L., Morel, J.-M., 2008. *From Gestalt Theory to Image Analysis*. Vol. 34. Springer New York.
- Du, K.-L., Swamy, M., 2014. Principal component analysis. In: *Neural Networks and Statistical Learning*. Springer London, pp. 355–405.
- E.R.S., E. R. I., January 2014. Sketch maps of extensional structures.
URL <http://www.europlanet-ri.eu/>
- ERSDAC, E. R. S. D. A. C., 2005. Aster User's Guide ver.4.0.
- Fallatah, A., 2011. Detection of linear segments in multispectral satellite images of urban area based on Helmholtz principle. diploma thesis, University of Twente Faculty of Geo-Information and Earth Observation (ITC), Enschede.
- Gómez, H., Kavzoglu, T., 2005. Assessment of shallow landslide susceptibility using artificial neural networks in Jabonosa River Basin, Venezuela. *Engineering Geology* 78, 11–27.
- Goodchild, M. F., Jeansoulin, R., 1998. Statistical representation of relative positional uncertainty for geographical linear features. In: *Data quality in geographic information: from error to uncertainty*. Editions Hermes, pp. 87–96.

- Grompone von Gioi, R., Jakubowicz, J., Morel, J.-M., Randall, G., 2012. LSD: a Line Segment Detector. *Image Processing On Line* 2012.
URL <http://www.ipol.im/pub/art/2012/gjmr-lsd/>
- Guru, D., Shekar, B., Nagabhushan, P., 2004. A simple and robust line detection algorithm based on small eigenvalue analysis. *Pattern Recognition Letters* 25 (1), 1 – 13.
- Hastie, T., Tibshirani, R., Friedman, J., 2009. Kernel smoothing methods. In: *The Elements of Statistical Learning*. Springer Series in Statistics. Springer New York, pp. 191–218.
- Heipke, C., Mayer, H., Wiedemann, C., Jamet, O., 1997. Evaluation of automatic road extraction. *International Archives of Photogrammetry and Remote Sensing* 32 (3 SECT 4W2), 151–160.
- Hobbs, W., 1904. Lineaments of the Atlantic border region 15, 480–506.
- Hung, L., Batelaan, O., De Smedt, F., 2005. Lineament extraction and analysis, comparison of landsat etm and aster imagery. case study: Suoimuoi tropical karst catchment, Vietnam. Vol. 5983.
- Karnieli, A., Meisels, A., Fisher, L., Arkin, Y., 1993. Automatic extraction and evaluation of geological linear features from digital remote sensing data using a Hough transform.
- Khomyakov, M., 2012. Comparative evaluation of linear edge detection methods. *Pattern Recognition and Image Analysis* 22 (2), 291–302.
- Koike, K., Nagano, S., Ohmi, M., 1995. Lineament analysis of satellite images using a segment tracing algorithm (sta). *Computers and Geosciences* 21 (9), 1091–1104.
- Kuria, Z., 2011. Seismotectonics of active faults : Magadi fault system, Southern Kenya rift. Ph.D. thesis, University of Twente Faculty of Geo-Information and Earth Observation (ITC).
- Lee, T., Moon, W., 2002. Lineament extraction from Landsat TM, JERS-1 SAR, and DEM for geological applications. Vol. 6. pp. 3276–3278.
- Mabee, S. B., Hardcastle, K. C., Wise, D. U., 1994. A method of collecting and analyzing lineaments for regional-scale fractured-bedrock aquifer studies. *Ground Water* 32 (6), 884–894.
- Marghany, M., Hashim, M., 2010. Lineament mapping using multispectral remote sensing satellite data. *International Journal of Physical Sciences* 5 (10), 1501–1507.
- Marghany, M., Mansor, S., Hashim, M., 2009. Geologic mapping of United Arab Emirates using multispectral remotely sensed data. *American Journal of Engineering and Applied Sciences* 2 (2), 476.
- Mavrantza, O., Argialas, D., 2002. Implementation and evaluation of spatial filtering and edge detection techniques for lineament mapping - case study: Alevrada, central greece. Vol. 4886. pp. 417–428.
- Mavrantza, O., Argialas, D., 2008. An object-oriented image analysis approach for the identification of geologic lineaments in a sedimentary geotectonic environment. In: *Object-Based Image Analysis*. Springer, pp. 383–398.
- McKeown, D. M., Bulwinkle, T., Cochran, S., Harvey, W., McGlone, C., Shufelt, J. A., 2000. Performance evaluation for automatic feature extraction. *International Archives of Photogrammetry and Remote Sensing* 33 (B2; PART 2), 379–394.

- Michaelsen, E., 2012. Perceptual grouping of row-gestalts in aerial NIR images of urban terrain.
- Mwakisunga, H., 2010. Gestalt theory for remote sensing image analysis. diploma thesis, University of Twente Faculty of Geo-Information and Earth Observation (ITC), Enschede.
- O'Leary, D. W., Friedman, J. D., Pohn, H. A., 1976. Lineament, linear, lineation: Some proposed new standards for old terms 87 (10), 1463–1469.
- Péteri, R., Couloigner, I., Ranchin, T., et al., 2004. Quantitatively assessing roads extracted from high-resolution imagery. *Photogrammetric Engineering & Remote Sensing* 70 (12), 1449–1456.
- Ramli, M., Yusof, N., Yusoff, M., Juahir, H., Shafri, H., 2010. Lineament mapping and its application in landslide hazard assessment: a review. *Bulletin of Engineering Geology and the Environment* 69 (2), 215–233.
- Sequar, G., 2009. Neotectonics of the east african rift system : new interpretations from conjunctive analysis of field and remotely sensed datasets in the lake Magadi area, Kenya. Diploma thesis, University of Twente Faculty of Geo-Information and Earth Observation (ITC), Enschede.
- Singhal, B., Gupta, R., 2010. Fractures and discontinuities. In: *Applied Hydrogeology of Fractured Rocks*.
- Song, W., Haithcoat, T. L., Hipple, J. D., 2001. An integrated approach of automatic road extraction and evaluation from remotely sensed imagery. Master's thesis, University of Missouri-Columbia.
- Thannoun, R. G., 2013. Automatic extraction and geospatial analysis of lineaments and their tectonic significance in some areas of Northern Iraq using remote sensing techniques and GIS. *International Journal of Enhanced Research in Science Technology and Engineering* 2 (2), 2548–2557.
- Vassilas, N., Perantonis, S., Charou, E., Tsenoglou, T., Stefouli, M., Varoufakis, S., 2002. Delineation of lineaments from satellite data based on efficient neural network and pattern recognition techniques. In: *2nd Hellenic Conf. on AI, SETN-2002*. Citeseer, pp. 11–12.
- Wang, J., Howarth, P., 1990. Use of the hough transform in automated lineament. *Geoscience and Remote Sensing, IEEE Transactions on* 28 (4), 561–567.
- Wladis, D., 1999. Automatic lineament detection using digital elevation models with second derivative filters. *Photogrammetric engineering and remote sensing* 65, 453–458.
- Woldai, T., October 2013. personal communication.
- Ziou, D., Tabbone, S., 1998. Edge detection techniques-an overview. *International Journal of Pattern Recognition and Image Analysis* 8, 537–559.